Inorganic Chemistry
Article
Cite This: Inorg. Chem. XXXX, XXX, XXX−XXX
pubs.acs.org/IC

Electron Paramagnetic Resonance Spectroscopy as a Probe of Hydrogen Bonding in Heme-Thiolate Proteins

Matthew R. Dent,[†] Michael W. Milbauer,[†] Andrew P. Hunt,[‡] Michael M. Aristov,[†] Ilia A. Guzei,[†] Nicolai Lehnert,[‡] and Judith N. Burstyn*[,†]

[†]Department of Chemistry, University of Wisconsin-Madison, 1101 University Avenue, Madison, Wisconsin 53706, United States
[‡]Department of Chemistry, University of Michigan, 930 North University Avenue, Ann Arbor, Michigan 48109, United States

Supporting Information

ABSTRACT: Despite utilizing a common cofactor binding motif, hemoproteins bearing a cysteine-derived thiolate ligand (heme-thiolate proteins) are involved in a diverse array of biological processes ranging from drug metabolism to transcriptional regulation. Though the origin of heme-thiolate functional divergence is not well understood, growing evidence suggests that the hydrogen bonding (H-bonding) environment surrounding the Fe-coordinating thiolate influences protein function. Outside of X-ray crystallography, few methods exist to characterize these critical H-bonding interactions. Electron paramagnetic resonance (EPR) spectra of heme-thiolate proteins bearing a six-coordinate, Fe(III) heme exhibit uniquely narrow low-spin (S = 1/2), rhombic signals, which are sensitive to changes in the heme-thiolate H-bonding environment. To establish a well-defined relationship between the magnitude of g-value dispersion in this unique EPR signal and the strength of the heme-thiolate H-bonding environment, we synthesized and characterized of a series of six-coordinate, aryl-thiolate-ligated Fe(III) porphyrin complexes bearing a tunable intramolecular H-bond. Spectroscopic investigation of these complexes revealed a direct correlation between H-bond strength and g-value dispersion in the rhombic EPR signal. Using density functional theory (DFT), we elucidated the electronic origins of the narrow, rhombic EPR signal in heme-thiolates, which arises from an Fe−S p_π−d_π bonding interaction. Computational analysis of the intramolecularly H-bonded heme-thiolate models revealed that H-bond donation to the coordinating thiolate reduces thiolate donor strength and weakens this Fe−S interaction, giving rise to larger g-value dispersion. By defining the relationship between heme-thiolate electronic structure and rhombic EPR signal, it is possible to compare thiolate donor strengths among heme-thiolate proteins through analysis of low-spin, Fe(III) EPR spectra. Thus, this study establishes EPR spectroscopy as a valuable tool for exploring how second coordination sphere effects influence heme-thiolate protein function.

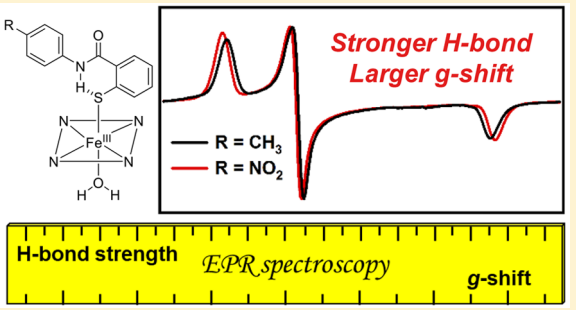

1. INTRODUCTION

Hemoproteins bearing an axial, cysteine-derived thiolate ligand (heme-thiolate proteins) are an important class of metalloproteins with diverse biological functions ranging from drug metabolism to transcriptional regulation. Importantly, properties of the b-type heme cofactor that give rise to diverse biological functions in heme-thiolate proteins also impart distinct spectroscopic characteristics. These properties include sixth axial ligand identity, iron coordination number and spin state, solvent exposure, and the propensity to react with substrates or bind small gaseous molecules. Two classes of heme-thiolate proteins emerge based on these functional and spectroscopic features: type-1 heme-thiolates, which act as *small-molecule activators*, and type-2 heme-thiolates, which act primarily as *small molecule sensors*.[1]

We hypothesize that a key contributing factor to functional divergence in heme-thiolate proteins is the structure of the hydrogen-bonding (H-bonding) environment surrounding the coordinating Cys(thiolate) (Cys(S^-)) ligand. A well-defined H-bonding pocket envelops the heme-bound Cys(S) in cytochrome P450 enzymes (a large group of type-1 heme-thiolate proteins), and a growing body of work implicates this H-bonding network in maintaining stability of the Fe−S bond and in modulating reactivity of the heme.[2−10] In a number of type-2 heme-thiolate proteins, H-bonding interactions may facilitate ligand switching at the heme,[11−14] although structural characterization of these interactions is limited.

Type-1 heme-thiolate proteins, which include a number of small-molecule-activating enzymes such as cytochromes P450 (Cyt P450s), chloroperoxidases, and nitric oxide synthases/reductases, possess a well-characterized H-bonding network that stabilizes thiolate coordination and modulates heme reactivity. In the exemplar camphor-hydroxylating $P450_{cam}$ from *Pseudomonas putida*, three amide N−H groups from three amino acid residues (Leu^{358}, Gly^{359}, and Gln^{360}) act as H-bond donors to the Cys(S^-) ligand (Cys^{357}) (Figure 1, left).[15−18] Additionally, the side chain amide of Gln^{360} serves as

Received: August 19, 2019

DOI: 10.1021/acs.inorgchem.9b02506
Inorg. Chem. XXXX, XXX, XXX−XXX

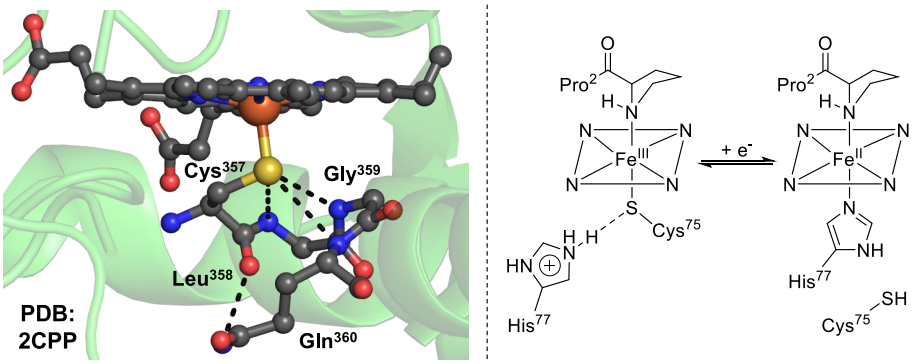

Figure 1. Comparison of heme-thiolate H-bonding environments in archetypical type-1 and type-2 heme-thiolate proteins. Left: Crystal structure of the thiolate H-bonding pocket in Cyt $P450_{cam}$ from *P. putida*, a type-1 heme-thiolate.[15] Residues involved in the thiolate H-bonding pocket are labeled, and important H-bonds are depicted as black dashes. Donor−acceptor distances range from 3.08 to 3.56 Å. Structure was visualized using Pymol (v1.3). Right: Proposed H-bonding environment in *Rr* CooA, a type-2 heme-thiolate.

Table 1. Comparison of Experimental *g*-Values for Low-Spin, Rhombic EPR Signals Observed in Fe(III) Hemoproteins[a]

protein	axial heme ligands	g_z	g_y	g_x	ref
cytochrome b_5	His/His	3.03	2.21	1.40	33
cytochrome *c*	His/Met	3.08	2.14	1.35	34
hCBS	$Cys(S^-)$/His	2.49	2.31	1.87	35
*Px*RcoM-1	$Cys(S^-)$/His	2.48	2.26	1.88	28
*Rr*CooA	$Cys(S^-)$/Pro	2.46	2.25	1.89	30
cyt $P450_{cam}$	$Cys(S^-)/H_2O$	2.41	2.26	1.93	4
cyt $P450_{cam}$ + imidazole (Im)	$Cys(S^-)$/Im	2.56	2.27	1.87	36

[a]Historical assignments of g_{max}, g_{mid}, and g_{min} are given as g_z, g_y, and g_x in this table.

a H-bond donor to the carbonyl O atom of Cys^{357}. Synthetic model studies highlight the importance of this H-bonding environment: Varying the number of H-bonds to thiolate modulates Fe−S covalency and influences the redox potential of thiolate-ligated porphyrins.[19−21] In Cyt P450 proteins, disruptions to this H-bonding pocket give rise to increased formation of the inactive, thiolate-protonated P420 species via weakening the Fe−S bond.[4−6] Thus, an important role of the thiolate H-bonding network is to maintain the thiolate coordination that is critical in (1) facilitating O−O bond cleavage of the hydroperoxo intermediate via the "thiolate-push" effect and (2) increasing the basicity of the protonated ferryl species in compound II.[2,3,22−26] Hunt and Lehnert recently elucidated the electronic origin of the thiolate-push effect in synthetic models of cytochrome P450 nitric oxide reductase.[10] They found that the thiolate ligand exhibits a strong σ-trans effect, which attenuates Fe−NO and N−O bond strengths in Fe(III) heme-thiolate nitrosyl adducts through population of an antibonding Fe−N−O σ^* orbital. DFT calculations demonstrated that the O−O bond in Compound 0 of the Cyt P450 monooxygenase catalytic cycle is also weakened via this thiolate σ-trans effect. Importantly, this study demonstrated that thiolate σ-donor strength, a property that may be tuned via changes in the thiolate H-bonding environment, directly modulates the strength of the σ-trans effect.

The thiolate H-bonding environment in type-2 heme-thiolate proteins likely facilitates redox-mediated ligand switching and may differ significantly from the environment in type-1 heme thiolate proteins. Type-2 heme-thiolate proteins are often small-molecule sensors involved in signal-dependent transcriptional regulation.[1] The type-2 heme exists as a low-spin species with two axial ligands; however, a "redox-mediated ligand switch" occurs in which the thiolate ligand is replaced with another protein-derived ligand upon reduction from Fe(III) to Fe(II).[11,12,27,28] A second change in heme coordination, in which a small molecule replaces an axial protein-derived ligand, occurs at the six-coordinate, Fe(II) heme *only after* the thiolate ligand is replaced. Binding of a small gaseous molecule (such as carbon monoxide or nitric oxide) to heme allosterically modulates protein function, often leading to enhanced binding to a DNA promoter site.[29−31] In the archetypical type-2 heme-thiolate protein, CooA (CO oxidation activator), we speculate that a strong, directional H-bond may exist between the coordinating Cys^{75} and the protonated imidazolium ring of His^{77} (Figure 1, right); in support of this hypothesis, distinct changes in the EPR spectrum of the low-spin, Fe(III) heme are observed upon mutation of His^{77} to Tyr.[12] No crystal structure of CooA with heme in the Fe(III) state currently exists, possibly due to the dynamic nature of this protein in the inactive state.[32] There are limited crystallographic data for type-2 heme-thiolate proteins in general; therefore, it is difficult to compare and contrast thiolate H-bonding networks between type-1 and type-2 proteins. This limitation precludes a comprehensive assessment of the role of thiolate H-bonding in the functional differentiation between these protein types.

Ferric heme-thiolate proteins exhibit a rhombic, low-spin ($S = 1/2$), electron paramagnetic resonance (EPR) signal with characteristically small shifts from $g_e \sim 2.00$ (*g*-shifts). Table 1 summarizes the set of *g*-values for a number of hemeproteins with different axial ligands. Hemoproteins with axial His/His (cytochrome b_5) and His/Met ligation (cytochrome *c*) exhibit a very anisotropic, rhombic signal with *g*-values in the range of $g \approx 3.1-1.35$.[33,34] In contrast, heme-thiolate proteins exhibit a rhombic signal with significantly less *g* anisotropy, with *g*-values

DOI: 10.1021/acs.inorgchem.9b02506
Inorg. Chem. XXXX, XXX, XXX−XXX

in a very narrow range between $g \approx 2.5$ and 1.9.[4,28,30,35,36] Blumberg and Peisach noted the unique features of heme-thiolate proteins in their analysis of low-spin, Fe(III) hemoprotein EPR spectra in the 1970s, and the characteristic EPR signal facilitated the identification of Cys(S^-) as an axial heme ligand when Cyt P450s were originally characterized.[37−39] This unique rhombic signal continues to be useful in identifying new heme-thiolate proteins;[40] however, the underlying features of the heme electronic structure that give rise to low g anisotropy in heme-thiolate proteins have not been elucidated.

Herein, we uncover the electronic origins of the characteristically small g-shifts observed in rhombic EPR spectra of low-spin, Fe(III) heme-thiolate proteins. Additionally, we establish a relationship between the magnitude of the g-shift and heme-thiolate H-bond strength. We characterize a series of six-coordinate, aryl-thiolate-ligated Fe(III) porphyrin models bearing a tunable, intramolecular H-bond using computational and spectroscopic methods. Our findings demonstrate that EPR spectroscopy, which is extremely sensitive to changes in Fe−S bonding, is particularly well-suited to probe second coordination sphere effects in heme-thiolate proteins. Specifically, we show that EPR spectroscopy reports on the strength of the thiolate H-bonding environment and therefore represents an important tool for understanding how this critical second coordination sphere effect influences heme-thiolate protein function.

2. EXPERIMENTAL SECTION

2.1. General Methods. Unless otherwise specified, reagents were used as received from commercial suppliers (Sigma-Aldrich, Acros Organics, Alfa Aesar, and Cambridge Isotope Laboratories, Inc.). The preparation and handling of all O_2- and H_2O-sensitive materials was carried out under inert conditions (N_2 or Ar gas) using standard Schlenk techniques or in an N_2-atmosphere MBraun glovebox equipped with a circulating purifier (O_2, H_2O < 0.1 ppm). For procedures involving the synthesis of thiol ligand precursors, solvents were dried by elution through alumina. For procedures involving porphyrin complexes, all dry solvents were distilled from CaH_2 under N_2, degassed via five freeze−pump−thaw cycles, and stored over appropriately sized (3 or 4 Å) activated molecular sieves in a glovebox until used, unless otherwise stated.

2.2. Physical Measurements. *2.2.1. Electronic Absorption Spectroscopy.* An Analytik Jena Specord S600 spectrometer was used to record electronic absorption spectra of solutions in anaerobic screw-cap quartz cuvettes, which were prepared in a glovebox.

2.2.2. NMR Spectroscopy. Proton and fluorine NMR spectra were recorded on a Bruker Avance III 500 MHz instrument or on Varian NMRS 500 or 700 MHz spectrophotometers at room temperature (20−22 °C). All spectra were referenced to internal solvent peaks (e.g., CD_2Cl_2: 5.32 ppm).

2.2.3. EPR Spectroscopy. Electron paramagnetic resonance (EPR) spectra were recorded on a Bruker X-band EMX or ELEXSYS E500 spectrophotometer equipped with an Oxford Instruments liquid helium cryostat. EPR spectra were obtained on frozen solution samples (0.5−2 mM) in a 1:1 mixture of CH_2Cl_2 and toluene, using 1−20 mW microwave power and 100 kHz field modulation with the amplitude set to 3 or 8.3 G. The g-values for each EPR spectrum were extracted from simulations performed using EasySpin (v5.2.23).[41]

2.2.4. Elemental Analysis. Elemental analyses (C, H, and N) were performed at Atlantic Microlab.

2.2.5. Mass Spectrometry. High-resolution mass spectrometry (HRMS) experiments were carried out using a Thermo Q Exactive Plus electrospray ionization-quadrupole-ion trap mass spectrometer.

2.3. Syntheses. *2.3.1. General Procedure for the Synthesis of 2,2′-Disulfanediylbis(N-phenylbenzamide) (**SS**-H) and Derivatives.* Oxalyl chloride (4 mL, 47 mmol, 2.6 equiv) was added to a suspension of 2,2′-disulfanediyldibenzoic acid (5.5 g, 18.0 mmol) and catalytic dimethylformamide in CH_2Cl_2 (75 mL) at room temperature. The reaction mixture was heated to reflux and stirred for 4 h until no solids remained. The reaction mixture was then hot-filtered, and solvent was removed from the collected filtrate *in vacuo*. The resulting amber, crystalline solid was used without further purification. Aniline (0.8 mL, 8.7 mmol, 3 equiv) was added slowly to a suspension of 2,2′-disulfanediyldibenzoyl chloride (1.00 g, 2.9 mmol) and $NaHCO_3$ (0.979 g, 11.7 mmol, 4 equiv) in CH_2Cl_2 (30 mL), and the reaction mixture was stirred overnight at room temperature. The precipitate was collected by vacuum filtration, suspended in HCl (aqueous; 3.7%, 40 mL) and stirred for 15 min. Solids were collected by vacuum filtration and washed with Et_2O (40 mL) to afford 2,2′-disulfanediylbis(*N*-phenylbenzamide) as an off-white solid. ^{1}H NMR (DMSO-d_6) δ 10.57 (s, 2H), 7.81−7.73 (m, 8H), 7.52 (td, J = 7.7, 1.5 Hz, 2H), 7.43−7.36 (m, 6H), 7.17−7.10 (m, 2H). ^{13}C NMR (126 MHz, DMSO-d_6) δ 166.17, 139.33, 136.92, 135.17, 131.91, 129.22, 128.95, 126.84, 126.74, 124.46, 120.60. ESI-MS [M + Na]$^+$: 479.0864 (calcd), 479.0825 (exptl). Yield: 1.17 g (2.6 mmol), 87%.

*2.3.1.1. 2,2′-Disulfanediylbis(N-(p-tolyl)benzamide) (**SS**-CH_3).* *p*-Toluidine (0.937 g, 8.7 mmol, 3 equiv) was used as a starting material following the general procedure above to afford 2,2′-disulfanediylbis-(*N*-(*p*-tolyl)benzamide) as an off-white solid. ^{1}H NMR (400 MHz, DMSO-d_6) δ 10.48 (s, 2H), 7.77 (dd, J = 7.7, 1.4 Hz, 2H), 7.74 (dd, J = 8.1, 1.1 Hz, 2H), 7.65 (d, J = 8.2 Hz, 4H), 7.51 (td, J = 7.7, 1.5 Hz, 2H), 7.39 (td, J = 7.4, 1.2 Hz, 2H), 7.18 (d, J = 8.2 Hz, 4H), 2.30 (s, 6H). ^{13}C NMR (126 MHz, DMSO-d_6) δ 165.47, 136.45, 136.34, 134.71, 132.96, 131.34, 129.11, 128.40, 126.31, 126.20, 120.11, 20.52. ^{13}C NMR (126 MHz, DMSO-d_6) δ 165.95, 136.93, 136.82, 135.19, 133.43, 131.82, 129.59, 128.88, 126.79, 126.68, 120.59, 21.00. ESI-MS [M + Na]$^+$: 507.1177 (calcd), 507.1152 (exptl). HRMS (+ESI) m/z: [M + Na]$^+$ Calculated for $C_{28}H_{24}N_2O_2S_2Na$: 507.1177. Found: 507.1152. Yield: 1.23 g (2.5 mmol), 85%.

*2.3.1.2. 2,2′-Disulfanediylbis(N-(4-chlorophenyl)benzamide) (**SS**-Cl).* 4-Chloroaniline (1.16 g, 8.7 mmol, 3 equiv) was used as a starting material following the general procedure above to afford 2,2′-disulfanediylbis(*N*-(4-chlorophenyl)benzamide) as an off-white solid. ^{1}H NMR (DMSO-d_6) δ 10.71 (s, 2H), 7.86−7.77 (m, 6H), 7.75 (dd, J = 8.1, 1.1 Hz, 2H), 7.53 (td, J = 7.7, 1.5 Hz, 2H), 7.47−7.43 (m, 4H), 7.40 (td, J = 7.5, 1.1 Hz, 2H). ^{13}C NMR (126 MHz, DMSO-d_6) δ 166.22, 138.29, 136.96, 134.84, 132.07, 129.15, 129.04, 128.07, 126.90, 126.82, 122.12. ESI-MS [M + Na]$^+$: 547.0084 (calcd), 547.0078 (exptl). HRMS (+ESI) m/z: [M + Na]$^+$ Calculated for $C_{26}H_{18}Cl_2N_2O_2S_2Na$: 547.0084. Found: 547.0078. Yield: 1.39 g (2.7 mmol), 91%.

*2.3.1.3. 2,2′-Disulfanediylbis(N-(4-(trifluoromethyl)phenyl)-benzamide) (**SS**-CF_3).* 4-(Trifluoromethyl)aniline (1.1 mL, 8.7 mmol, 3 equiv) was used as a starting material following the general procedure above to afford 2,2′-disulfanediylbis(*N*-(4-(trifluoromethyl)phenyl)benzamide) as an off-white solid.^{1}H NMR (DMSO-d_6) δ 10.92 (s, 2H), 7.99 (d, J = 8.6 Hz, 4H), 7.83 (dd, J = 7.7, 1.4 Hz, 2H), 7.78−7.75 (m, 6H), 7.55 (td, J = 7.7, 1.4 Hz, 2H), 7.42 (td, J = 7.5, 1.1 Hz, 2H). ^{13}C NMR (126 MHz, DMSO-d_6) δ 166.16, 142.47, 136.56, 134.19, 131.81, 128.77, 126.53, 126.49, 126.08 (q, J = 3.9 Hz), 124.37 (q, J = 271.3 Hz), 123.97 (q, J = 32.0 Hz), 120.04. HRMS (+ESI) m/z: [M + Na]$^+$ Calculated for $C_{28}H_{18}F_6N_2O_2S_2Na$: 615.0612. Found: 615.0598. Yield: 1.61 g (2.7 mmol), 93%.

*2.3.1.4. 2,2′-Disulfanediylbis(N-(4-nitrophenyl)benzamide) (**SS**-NO_2).* The general procedure was modified by heating the reaction to reflux and stirring for 2 days following the addition of 4-nitroaniline (1.21 g, 8.7 mmol, 3 equiv). 2,2′-Disulfanediylbis(*N*-(4-nitrophenyl)-benzamide) was obtained as an off-white solid. ^{1}H NMR (DMSO-d_6) δ 11.13 (s, 2H), 8.32−8.27 (m, 4H), 8.03 (d, J = 9.3 Hz, 4H), 7.86 (dd, J = 7.6, 1.5 Hz, 2H), 7.81−7.76 (m, 2H), 7.57 (td, J = 7.8, 1.5 Hz, 2H), 7.47−7.41 (m, 2H). ^{13}C NMR (126 MHz, DMSO-d_6) δ 166.31, 145.04, 142.74, 136.66, 133.90, 132.03, 128.92, 126.62, 126.60, 124.93, 119.81. HRMS (+ESI) m/z: [M + Na]$^+$ Calculated for $C_{26}H_{18}N_4O_6S_2Na$: 569.0565. Found: 569.0561. Yield: 1.25 g (2.3 mmol), 77%.

DOI: 10.1021/acs.inorgchem.9b02506
Inorg. Chem. XXXX, XXX, XXX−XXX

*2.3.1.5. 2-Mercapto-N-phenylbenzamide (**HS**-H, Method A).* 2,2′-Disulfanediylbis(*N*-phenylbenzamide) (456 mg, 1 mmol) and triphenylphosphine (1.18 g, 4.5 mmol) were suspended in a 50/50 mixture of CH_3CN/H_2O and stirred at reflux for 1 h. The suspension was then added to a separatory funnel and mixed with NaCl (aqueous) brine (15 mL) and hexanes (15 mL). The middle CH_3CN layer was collected and dried with $MgSO_4$, and solvent was removed *in vacuo*. The crude solid was purified by silica column chromatography (100% CH_2Cl_2) to afford 2-mercapto-*N*-phenylbenzamide as a white solid. ^{1}H NMR (500 MHz, $CDCl_3$) δ 7.77 (s, 1H), 7.61 (d, J = 8.0 Hz, 2H), 7.58 (dd, J = 7.7, 1.5 Hz, 1H), 7.39−7.34 (m, 3H), 7.30 (td, J = 7.6, 1.5 Hz, 1H), 7.22−7.14 (m, 2H), 4.56 (s, 1H). ^{13}C NMR (126 MHz, $CDCl_3$) δ 166.59, 137.61, 133.55, 132.98, 131.39, 131.01, 129.14, 128.03, 125.50, 124.87, 120.25. HRMS (+ESI) m/z: $[M + H]^+$ Calculated for $C_{13}H_{12}NOS$: 228.0489. Found: 228.0489. Yield: 395 mg (1.7 mmol), 86%.

*2.3.1.6. 2-Mercapto-N-(p-tolyl)benzamide (**HS**-CH_3).* 2,2′-Disulfanediylbis(*N*-(*p*-tolyl)benzamide) (485 mg, 1 mmol) was used as a starting material following Method A above to afford 2-mercapto-*N*-(*p*-tolyl)benzamide as a white solid. ^{1}H NMR ($CDCl_3$) δ 7.65 (s, 1H), 7.58 (d, J = 7.6 Hz, 1H), 7.50 (d, J = 7.9 Hz, 2H), 7.38 (dd, J = 7.8, 1.3 Hz, 1H), 7.31 (td, J = 7.6, 1.5 Hz, 1H), 7.22 (dd, J = 7.6, 1.3 Hz, 1H), 7.19 (t, J = 7.1 Hz, 2H), 4.62 (s, 1H), 2.35 (s, 3H).). ^{13}C NMR (126 MHz, chloroform-*d*) δ 166.69, 135.15, 134.64, 133.66, 133.04, 131.36, 130.97, 129.67, 128.14, 125.50, 120.49, 21.03. HRMS (+ESI) m/z: $[M + H]^+$ Calculated for $C_{14}H_{14}NOS$: 242.0645. Found: 242.0645. Yield: 482 mg (2.0 mmol), 99%.

*2.3.1.7. 2-Mercapto-N-(4-chlorophenyl)benzamide (**HS**-Cl).* 2,2′-Disulfanediylbis(*N*-(4-chlorophenyl)benzamide) (525 mg, 1 mmol) was used as a starting material following Method A above to afford 2-mercapto-*N*-(4-chlorophenyl)benzamide as a white solid. ^{1}H NMR (500 MHz, $CDCl_3$) δ 7.79 (s, 1H), 7.59−7.53 (m, 3H), 7.37 (dd, J = 7.9, 1.3 Hz, 1H), 7.35−7.29 (m, 3H), 7.21 (td, J = 7.5, 1.3 Hz, 1H), 4.48 (s, 1H). ^{13}C NMR (126 MHz, $CDCl_3$) δ 166.50, 136.19, 133.20, 133.01, 131.55, 131.22, 129.90, 129.16, 128.05, 125.59, 121.46. HRMS (+ESI) m/z: $[M + H]^+$ Calculated for $C_{13}H_{11}ClNOS$: 262.0099. Found: 262.0097. Yield: 384 mg (1.5 mmol), 73%.

*2.3.1.8. 2-Mercapto-N-(4-(trifluoromethyl)phenyl)benzamide (**HS**-CF_3, Method B).* 2,2′-Disulfanediylbis(*N*-(4-(trifluoromethyl)-phenyl)benzamide) (593 mg, 1 mmol) and $NaBH_4$ (378 mg, 10 mmol) were placed in an oven-dried flask and evacuated and refilled with N_2 three times. Methanol (15 mL) was added slowly to prevent vigorous bubbling, and the resulting reaction mixture was stirred for 1 h at ambient temperature. Methanol was then removed *in vacuo*, and the resulting solid was redissolved in ethyl acetate (20 mL). This solution was stirred with HCl (aqueous; 7%, 20 mL) for 1 h. The compound of interest was extracted from this mixture into ethyl acetate (2 × 10 mL). Combined organic layers were dried over $MgSO_4$ and solvent was removed *in vacuo*. The crude solid was purified by silica column chromatography (100% CH_2Cl_2) to afford 2-mercapto-*N*-(4-(trifluoromethyl)phenyl)benzamide as a white solid. ^{1}H NMR (400 MHz, $CDCl_3$) δ 7.88 (s, 1H), 7.76 (d, J = 8.4 Hz, 2H), 7.63 (dd, J = 9.0, 7.4 Hz, 3H), 7.41 (dd, J = 7.8, 1.4 Hz, 1H), 7.35 (td, J = 7.6, 1.5 Hz, 1H), 7.28−7.23 (m, 2H), 4.44 (s, 1H). ^{13}C NMR (126 MHz, chloroform-*d*) δ 166.79, 140.82, 133.22, 133.10, 131.80, 131.56, 128.25, 126.72 (q, J = 32.9 Hz), 126.52, 125.80, 124.16 (q, J = 271.7 Hz), 119.93. ^{19}F NMR (471 MHz, chloroform-*d*) δ −62.19. HRMS (+ESI) m/z: $[M + H]^+$ Calculated for $C_{14}H_{11}F_3NOS$: 298.0508. Found: 298.0504. Yield: 164 mg (0.55 mmol), 55%.

*2.3.1.9. 2-Mercapto-N-(4-nitrophenyl)benzamide (**HS**-NO_2).* 2,2′-Disulfanediylbis(*N*-(4-nitrophenyl)benzamide) (547 mg, 1 mmol) was used as a starting material following Method B above to afford 2-mercapto-*N*-(4-nitrophenyl)benzamide as a pale yellow microcrystalline solid. ^{1}H NMR (400 MHz, $CDCl_3$) δ 8.28−8.22 (m, 2H), 8.18 (s, 1H), 7.85−7.80 (m, 2H), 7.63 (dd, J = 7.7, 1.5 Hz, 1H), 7.41 (dd, J = 7.9, 1.4 Hz, 1H), 7.36 (td, J = 7.6, 1.5 Hz, 1H), 7.28−7.22 (m, 1H), 4.35 (s, 1H). ^{13}C NMR (126 MHz, chloroform-*d*) δ 166.63, 144.09, 143.55, 133.37, 132.71, 132.08, 131.91, 128.36, 125.99, 125.33, 119.64. HRMS (−ESI) m/z: $[M - H]^-$ Calculated for $C_{13}H_9N_2O_3S$: 273.0339. Found: 273.0640. Yield: 343 mg (1.3 mmol), 62%.

2.3.2. General Procedure for the Synthesis of Five-Coordinate, Fe(III) Thiolate-Ligated Porphyrin Complexes. All iron-containing tetraphenylporphyrinate (TPP^{2-}) complexes were prepared using the same general procedure recently described for the synthesis of high-spin, five-coordinate [Fe(TPP)(**S**-R)] complexes, by mixing the desired thiol ligand precursor with $[Fe(TPP)(OCH_3)]$.[10] All complexes were recrystallized by dissolution in a minimal amount of toluene, followed by layering of the solutions with hexanes and/or methanol.

*2.3.2.1. [Fe(TPP)(**S**-CH_3)].* Electronic absorption (CH_2Cl_2): 380 (shoulder), 407, 515, 576, 719 nm. ^{1}H NMR (CD_2Cl_2): 71.4 (br, *β*-pyrrole H), 64.1 and 56.4 (s, *meta*-SPh's), 12.7 (br-s, *meta*-Ph TPP), 9.6 (br-s, *ortho*-Ph TPP), 6.9 (br-s, *para*-Ph TPP), 4.1 (s, SPh-NHPh-*para*-CH_3), −85.2 (s, *para*-SPh), −92.6 (br, *ortho*-SPh) ppm. Other SPh-NHPh-*p*CH_3 signals observed: 8.3 (br), 4.8 (br) and −109.9 (br) ppm. Anal. Calcd for $C_{58}H_{40}FeN_5OS$: C, 76.48; H, 4.43; N, 7.69. Found: C, 76.35; H, 4.47; N, 7.61. Yield: 47.9 mg, 78.8% (starting $[Fe(TPP)(OCH_3)]$ mass was 46.66 mg). EPR (1:1 CH_2Cl_2/toluene): g_x = 1.95, g_y = 1.88, g_z = 2.04; E/D = 0.040.

*2.3.2.2. [Fe(TPP)(**S**-H)].* Electronic absorption (CH_2Cl_2): 380 (shoulder), 407, 515, 576, 717 nm. ^{1}H NMR (CD_2Cl_2): 71.6 (br, *β*-pyrrole H), 63.7 and 56.5 (s, *meta*-SPh's), 12.8 (br-s, meta-Ph TPP), 9.8 (br-s, *ortho*-Ph TPP), 6.9 (br-s, para-Ph TPP), 6.5 (s, SPh-NHPh-para-H), −85.2 (s, *para*-SPh), −92.8 (br, *ortho*-SPh) ppm. Other SPh-NHPh signals observed: 8.3 (br), 4.9 (br) and −111.3 (br) ppm. Anal. Calcd for $C_{57}H_3FeN_5OS$: C, 76.34; H, 4.27; N, 7.81. Found: C, 75.66; H, 4.29; N, 7.62. Yield: 117.6 mg, 77.8% (starting $[Fe(TPP)(OCH_3)]$ mass was 101.4 mg). EPR (1:1 CH_2Cl_2/toluene): g_x = 1.95, g_y = 1.88, g_z = 2.085; E/D = 0.034.

*2.3.2.3. [Fe(TPP)(**S**-Cl)].* Electronic absorption (CH_2Cl_2): 380 (shoulder), 408, 515, 578, 720 nm. ^{1}H NMR (CD_2Cl_2): 71.5 (br, *β*-pyrrole H), 62.5 and 55.6 (s, *meta*-SPh's), 12.8 (br-s, *meta*-Ph TPP), 9.6 (br-s, *ortho*-Ph TPP), 6.8 (br-s, *para*-Ph TPP), −84.5 (s, *para*-SPh), −91.9 (br, *ortho*-SPh) ppm. Other SPh-NHPh-*p*Cl signals observed: 8.3 (br), 4.8 (br), and −111.6 (br) ppm. Anal. Calcd for $C_{57}H_{37}ClFeN_5OS$: C, 73.51; H, 4.00; N, 7.52; S, 3.44. Found: C, 72.21; H, 4.07; N 7.42, S, 3.60. Yield: 32.8 mg, 41.7% (starting $[Fe(TPP)(OCH_3)]$ mass was 59.1 mg). EPR (1:1 CH_2Cl_2/toluene): g_x = 1.95, g_y = 1.88, g_z = 2.06; E/D = 0.034.

*2.3.2.4. [Fe(TPP)(**S**-CF_3)].* Electronic absorption (CH_2Cl_2): 380 (shoulder), 408, 515, 578, 721 nm. ^{1}H NMR (CD_2Cl_2): 68.4 (br, *β*-pyrrole H), 61.2 and 54.8 (s, *meta*-SPh's), 12.8 (br-s, *meta*-Ph TPP), 9.9 (br-s, *ortho*-Ph TPP), 6.9 (br-s, *para*-Ph TPP), −83.2 (s, *para*-SPh), −90.4 (br, *ortho*-SPh) ppm. Other SPh-NHPh-*p*CF_3 signals observed: 8.0 (br), 5.0 (br) and −110.5 (br) ppm. ^{19}F-NMR (CD_2Cl_2): −60.3 ppm. Anal. Calcd for $C_{58}H_{37}F_3FeN_5OS$: C, 72.20; H, 3.87; N, 7.26. Found: C, 71.66; H, 3.86; N, 7.26. Yield: 34.8 mg, 46.7% (starting $[Fe(TPP)(OCH_3)]$ mass was 54.0 mg). EPR (1:1 CH_2Cl_2/toluene): g_x = 1.93, g_y = 1.87, g_z = 2.06; E/D = 0.037.

*2.3.2.5. [Fe(TPP)(**S**-NO_2)].* Electronic absorption (CH_2Cl_2): 336 (shoulder), 380 (shoulder), 408, 516, 578, 722 nm. ^{1}H NMR (CD_2Cl_2): 70.5 (br, *β*-pyrrole H), 69.9 and 54.3 (s, *meta*-SPh's), 12.9 (br-s, *meta*-Ph TPP), 10.5 (br-s, *ortho*-Ph TPP), 6.9 (br-s, *para*-Ph TPP), −83.7 (s, *para*-SPh), −90.2 (br, *ortho*-SPh) ppm. Other SPh-NHPh-*p*NO_2 signals observed: 8.2 (br), 4.9 (br) and −112.4 (br) ppm. Anal. Calcd for $C_{57}H_{37}FeN_6O_3S$: C, 72.69; H, 3.96; N, 8.92. Found: C, 72.35; H, 3.75; N, 8.71. Yield: 87.5 mg, 64.0% (starting $[Fe(TPP)(OCH_3)]$ mass was 101.5 mg). EPR (1:1 CH_2Cl_2/toluene): g_x = 1.94, g_y = 1.95, g_z = 2.00, E/D = 0.048. Crystal data for $C_{57}H_{37}FeN_6O_3S$ (M = 941.83 g/mol): monoclinic, space group $P2_1/c$ (no. 14), a = 14.124(4) Å, b = 12.805(4) Å, c = 24.419(8) Å, β = 90.916(13)°, V = 4416(2) Å^3, Z = 4, T = 100.0 K, μ(Mo Kα) = 0.445 mm^{-1}, $Dcalc$ = 1.417 g/cm^3, 96775 reflections measured (2.884° ≤ 2θ ≤ 53.52°), 9382 unique (R_{int} = 0.0684, R_{sigma} = 0.0337) which were used in all calculations. The final R_1 was 0.0360 ($I > 2\sigma(I)$) and wR_2 was 0.0887 (all data). Detailed methods for X-ray crystallography and additional crystallographic data can be found in the Supporting Information.

DOI: 10.1021/acs.inorgchem.9b02506
Inorg. Chem. XXXX, XXX, XXX−XXX

Table 2. Experimental and DFT-Computed Metal-Ligand Bond Distances for Low-Spin, Fe(III) Hemoprotein Models

			experimental			computed		
protein	L_1	L_2	$d_{Fe-Npor}$ (Å)[a]	d_{Fe-L1} (Å)	d_{Fe-L2} (Å)	$d_{Fe-Npor}$ (Å)[a]	d_{Fe-L1} (Å)	d_{Fe-L2} (Å)
cytochrome b_5	His(N)	His(N)	1.988	2.075	2.003	2.008	1.997	1.996
cytochrome c	His(N)	Met(S)	2.005	2.037	2.351	2.002	2.009	2.338
hCBS/*Px*RcoM	His(N)	Cys(S^-)	2.010	2.210	2.281	2.011	2.104	2.186

[a]Average Fe−N bond distance for pyrrole N atoms.

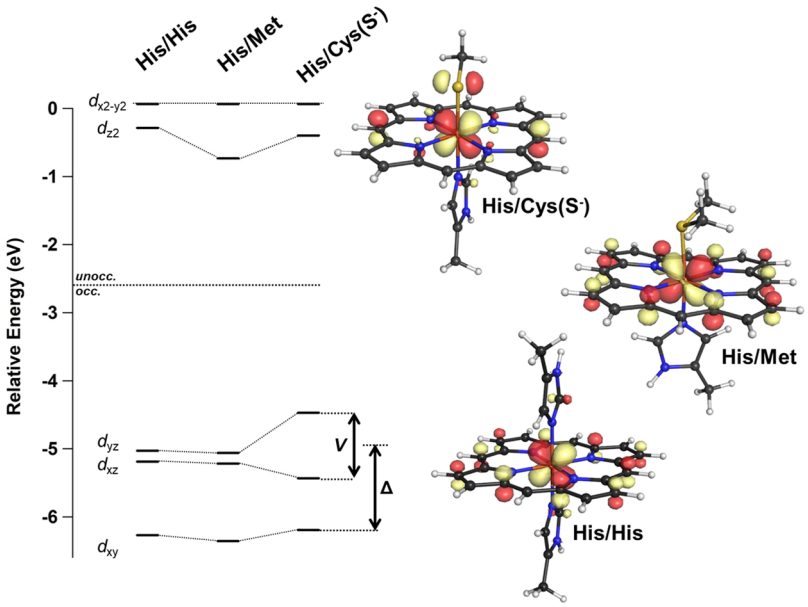

Figure 2. Electronic structure analysis of metal−ligand bonding in computational models of low-spin, Fe(III) porphyrins with different axial ligands. Left: The MO diagram depicts the relative energies of Fe 3d-based MOs (spin up, single-electron orbitals). Orbital energies are relative to the energy of the $3d_{x^2-y^2}$ orbital for each model. Two ligand field parameters, rhombic (V) and axial (Δ) splitting, are defined in terms of the relative energies of Fe $3d_{xy}$-, $3d_{xz}$-, and $3d_{yz}$-based MOs. Right: Geometry-optimized structures of each porphyrin model shown with an overlay of the Fe $3d_{yz}$-based, spin-down MO. Orbital plots were generated with an isosurface value of 0.05, and structures were visualized using Pymol (v1.3).

2.3.3. Preparation of Six-Coordinate, Fe(III) Thiolate-Ligated Porphyrin Complexes for EPR Spectroscopy. Six-coordinate (6-c) low-spin, Fe(III) porphyrin-thiolate complexes were prepared with either 1-methylimidazole (1-MeIm) or water as a second axial ligand. All complexes were prepared in EPR tubes in a glovebox. Porphyrin-thiolate complexes bound to 1-MeIm were prepared by mixing a solution of [Fe(TPP)(**S**-R)] (500 μM in 50:50 CH_2Cl_2/toluene) with 3 molar equiv of 1-MeIm. Porphyrin-thiolate complexes axially ligated by a water molecule were prepared by dissolving each 5-c compound in solvent (50:50 CH_2Cl_2/toluene) that had been dried only by elution through alumina and *without* further drying. The concentration of water in the solvent (≥2 mM, as determined by potentiometric titration) was such that it was in excess of the 5-c porphyrin species in each of these samples (500 μM).

2.4. Relationship between Experimentally Determined *g*-Values and Ligand Field Parameters. Ligand field parameters were estimated from experimentally determined g-values for low-spin, Fe(III) porphyrin models using the tetragonally distorted, strong field d^5 model described by McGarvey.[42] In the strong field approximation, the wave function for the ground state Kramers doublet ($^2T_{2g}$ in O_h symmetry) is modeled in terms of three low-lying, metal-based d-orbitals, d_{xy}, d_{xz}, and d_{yz}. The two other metal-based d-orbitals, d_{z^2} and $d_{x^2-y^2}$, are much higher in energy and therefore are not considered in this model. Wave function coefficients for each orbital (A, B, and C for d_{xy}, d_{yz}, and d_{xz}, respectively), as well as the orbital reduction factor k, are computed directly from experimentally determined values of g_x, g_y, and g_z. Two additional ligand field parameters, rhombic and axial distortions, are then computed from these wave function coefficients. The rhombic distortion (V/ξ), scaled to the single electron spin−orbit constant for Fe^{3+} (ξ = 464 cm^{-1}),[43] approximates the energy difference between Fe $3d_{xz}$ and $3d_{yz}$ orbitals (i.e., $E_{xz} = V/2 = -E_{yz}$). The axial distortion (Δ/ξ), scaled to ξ, approximates the energy difference between Fe $3d_{xy}$ and the barycenter of the $3d_{xz}$ and $3d_{yz}$ orbitals (i.e., $E_{xy} = \Delta$).

All ligand field parameters were computed using the program DLSD5, originally written by McGarvey,[42] as modified by Telser et al.[44] which systematically assigns the sign and magnitude of each g-value assuming maximal distortion along the z-axis (i.e., $|\Delta| \geq 2|V|/3$). For most low-spin, Fe(III) porphyrin complexes, the axis of maximal distortion lies normal to the heme plane and thus aligns with the molecular z-axis.[39] In this case, computed values for V/ξ and Δ/ξ were used directly. However, for thiolate-ligated porphyrins, the axis of maximal distortion lies *within* the heme plane, leading to an interchange of the x- and z-axes.[45] To provide meaningful information about electronic structure in terms of the molecular axes (in which z is normal to the heme plane), computed values for V/ξ and Δ/ξ in thiolate-ligated porphyrins were converted using eqs 1 and 2.

$$V' = 0.5V - \Delta \quad (1)$$

$$\Delta' = -0.5 - 0.75V \quad (2)$$

2.5. Computational Methods. *2.5.1. Density Functional Theory Calculations.* For 6-c, low-spin Fe(III) porphyrin models, geometry optimizations, single-point calculations, and time-dependent density functional theory (TD-DFT) computations were carried out using ORCA v4.0,[46] and frequency calculations were carried out using Gaussian09.[47] Geometry optimizations utilized Becke's functional for exchange along with Perdew's functional for correlation (BP86),[48,49] and all atoms were described using Alrich's polarized triple ζ-valence (TZVP) basis set along with the def2/J auxiliary basis.[50,51] Frequency

DOI: 10.1021/acs.inorgchem.9b02506
Inorg. Chem. XXXX, XXX, XXX−XXX

Table 3. Computational Analysis of Low-Spin, Fe(III) Hemoprotein Models[a]

protein	axial heme ligands	ΔE_1 (cm^{-1})	ΔE_2 (cm^{-1})	spin population			
				Fe $3d_{yz}$	Fe $3d_{xz}$	Fe $3d_{xy}$	S 3p
cytochrome b_5	His/His	3785	4118	0.4666	0.445	0.0316	N/A
cytochrome c	His/Met	2072	2571	0.6091	0.2863	0.04704	
hCBS	His/Cys(S^-)	5865	6379	0.7787	0.01453	0.03369	0.1565

[a]Values for ΔE_1 and ΔE_2 were computed using TD-DFT, and Löewdin spin populations were determined from single-point calculations.

calculations utilized Becke's three-parameter hybrid functional for exchange and the Lee−Yang−Parr functional for correlation (B3LYP), with the 6-31G(d) basis set.[52] Spin-unrestricted single-point calculations were performed using the B3LYP functional along with the polarized split valence potential (SVP) basis set and def2/J auxiliary basis for all atoms except Fe and S, which were modeled using the TZVPP basis set, and Fe-coordinated N atoms, which were modeled using the TZVP basis set.[51,53] Energy differences between ground and excited states were calculated using TD-DFT with the camB3LYP functional along with the polarized SVP basis set and def2/J auxiliary basis for all atoms except Fe and S, which were modeled using the TZVPP basis set, and Fe-coordinated N atoms, which were modeled using the TZVP basis set.

Initial coordinates for archetype hemoprotein models were obtained from protein crystal structures for cytochrome b_5 (PBD 1CYO),[54] cytochrome c (PBD 1CCR),[55] and human cystathionine β-synthase (PBD 1JBQ).[56] Histidine ligands were truncated at the β-methylene C atom, which was replaced with a methyl group, the methionine ligand was truncated at the γ-methylene C atom and replaced with a methyl group, and the cysteine ligand was truncated at the β-methylene C atom, which was replaced with a methyl group. Porphine (P^{2-}) was used to model all porphyrins by replacing porphyrin substituents with H atoms. Initial coordinates for synthetic models were derived from the crystal structure of [Fe(TPP)(**S**-NO_2)]. To generate starting coordinates for each 6-c compound, the *N*-phenyl *para*-substituent was modeled using idealized geometries, and a second axial ligand was added based on an appropriate crystal structure of a six-coordinate heme or porphyrin model complex.[56−58] To ensure proper positioning of the Fe atom in each model, the Fe atom was shifted to achieve coplanarity with the coordinating porphyrin N atoms in starting coordinates. All structural modifications were performed using the molecular builder in WebMO (v19.0.009e).[59] Geometry-optimized coordinates are compiled in Tables S9−S22.

3. RESULTS

3.1. Electronic Origins of the Unique Rhombic EPR Signal Associated with Low-Spin, Fe(III) Heme-Thiolate Proteins. We utilized density functional theory (DFT) computations to analyze metal−ligand bonding in three low-spin, Fe(III) hemoprotein models with His/His (cytochrome b_5), His/Met (cytochrome c), and His/Cys(S^-) (hCBS, *Px*RcoM) axial ligands. In all cases, the computed structures were consistent with those observed experimentally (Table 2). Axial metal−ligand bond distances were slightly (up to 0.1 Å) shorter than those observed experimentally, which is unsurprising given that the computational models do not account for secondary coordination sphere effects of the protein heme pocket. Using geometry-optimized model structures, we computed single-point energies and ground-state wave functions using DFT. We compared metal−ligand bonding in each of these hemoprotein models by examining the energies and orbital compositions of the predominantly Fe 3d-based frontier molecular orbitals (MOs) (Figure 2).

The orbital contributions to iron-ligand bonding were similar to one another in the His/His and His/Met models (Figures S3 and S4). In the case of the His/His model, the lowest energy Fe 3d-based MO was primarily d_{xy} in character. For the His/Met model, the lowest energy orbital was also predominantly Fe $3d_{xy}$ in character; however, there was also a significant contribution from a sulfur 3p orbital. This filled−filled π-type interaction results in no net Fe−S bonding character. The next lowest energy orbitals observed are the nearly degenerate Fe $3d_{xz}$- and $3d_{yz}$-based MOs, which both exhibit π-antibonding character with respect to the porphyrin p_z orbitals. The second-highest energy Fe 3d-based MO is largely d_{z^2} in character. This MO is primarily σ-antibonding with respect to the two axial heme ligands, is slightly σ-antibonding with respect to the porphyrin N atoms, and is slightly higher in energy in the His/His model than in the His/Met model. The highest energy Fe 3d-based MO in both models is largely $d_{x^2-y^2}$ in character and strongly σ-antibonding with respect to the porphyrin N atoms.

In the thiolate-bound His/Cys(S^-) model, the orbital contributions to axial iron-ligand bonding differ from those of the His/His and His/Met models. Specifically, one of the thiolate S 3p orbitals has the appropriate symmetry to engage in a $p_\pi-d_\pi$ bonding interaction with the Fe $3d_{yz}$ orbital (Figure S5). This bonding interaction raises the energy of the Fe $3d_{yz}$-based MO and lifts the near-degeneracy of d_{xz} and d_{yz} (Figure 2). Additionally, the energy of Fe $3d_{xz}$-based MO is lowered slightly, relative to those of the His/His and His/Met models.

Axial thiolate ligation to low-spin, Fe(III) heme increases the differences in energy between the ground state and two low-lying excited states. Using TD-DFT, we computed the differences in energy between the ground state and first two excited states in low-spin, Fe(III) hemoprotein models. Consistent with greater energy separation between Fe $3d_{xz}$- and $3d_{yz}$-based MOs, the energy of the $(d_{xy})^2(d_{xz})^2(d_{yz})^1 \rightarrow (d_{xy})^2(d_{xz})^1(d_{yz})^2$ transition (ΔE_1) increased substantially for the His/Cys(S^-) model (ΔE_1 = 5865 cm^{-1}) relative to His/His (ΔE_1 = 3785 cm^{-1}) and His/Met (ΔE_1 = 2072 cm^{-1}) models (Table 3). The energy of the $(d_{xy})^2(d_{xz})^2(d_{yz})^1 \rightarrow (d_{xy})^1(d_{xz})^2(d_{yz})^2$ transition (ΔE_2) also increased for the heme-thiolate model, consistent with a stronger overall axial ligand field.

Our computational results establish a connection between experimentally observed g-values and heme-thiolate electronic structure. In EPR spectroscopy, the shift from $g_e \sim 2.00$ arises from spin−orbit coupling of low-lying excited states into the paramagnetic ground state. The extent of this spin−orbit coupling cannot be directly calculated using DFT; however, spin−orbit coupling is inversely proportional to two parameters that can be estimated using computations: (1) metal−ligand covalency and (2) ground-state/excited-state energy differences. Our single-point DFT computations predict that thiolate ligation increases metal−ligand covalency, as indicated by the significant contribution of the sulfur 3p orbital to the unpaired spin population in the His/Cys(S^-) model (Table 3). This increased metal−ligand covalency likely diminishes spin−orbit coupling and contributes to the small

DOI: 10.1021/acs.inorgchem.9b02506
Inorg. Chem. XXXX, XXX, XXX−XXX

Table 4. Ligand Field Parameters Computed from Experimental *g*-Values for a Number of Hemoproteins with Varying Axial Ligands

protein	axial heme ligands	g_x	g_y	g_z	V/ξ[a]	$\lvert V\rvert$ (cm^{-1})[b]	Δ/ξ[c]	$\lvert\Delta\rvert$ (cm^{-1})[d]	k[e]	V/Δ[f]
cytochrome b_5	His/His	1.40	−2.21	−3.03	−1.63	750	−3.21	1477	1.01	0.51
cytochrome *c*	His/Met	1.35	−2.14	−3.08	−1.49	685	−3.39	1559	0.99	0.44
hCBS	$Cys(S^-)$/His	−2.48	−2.26	1.88	−4.32	1987	−5.03	2314	1.05	0.86
*Px*RcoM-1	$Cys(S^-)$/His	−2.49	−2.31	1.87	−4.39	2019	−4.26	1960	1.10	1.03
*Rr*CooA	$Cys(S^-)$/Pro	−2.46	−2.25	1.89	−4.51	2075	−5.24	2410	1.05	0.86
cyt $P450_{cam}$	$Cys(S^-)/H_2O$	−2.41	−2.26	1.93	−5.98	2751	−6.01	2765	1.22	0.99
cyt $P450_{cam}$ + imidazole (Im)	$Cys(S^-)$/Im	−2.56	−2.27	1.87	−4.06	1868	−5.46	2512	1.15	0.74

[a] V/ξ = rhombic splitting, V'/ξ for thiolate-ligated species, ξ = 460 cm^{-1} [b] $|V'|$ for thiolate-ligated species [c] Δ/ξ= axial splitting, Δ'/ξ for thiolate-ligated species [d] $|\Delta'|$ for thiolate-ligated species [e] k = orbital reduction factor [f] V/Δ = rhombicity, V'/Δ' for thiolate-ligated species

g-shifts observed in EPR spectra of heme-thiolate proteins. We qualitatively estimated ground-state/excited-state energy differences in low-spin, Fe(III) porphyrins by comparing the DFT-calculated ground state energies of Fe 3d-based MOs: Thiolate-ligated porphyrins exhibit large differences in energy between d_{xy}-, d_{xz}-, and d_{yz}-based MOs and therefore experience diminished spin−orbit coupling. TD-DFT computations are consistent with this trend: Thiolate ligation gives rise to an *increase* in ground state-excited state energy differences (ΔE_1 and ΔE_2) and thereby *attenuates* spin−orbit coupling in low-spin, Fe(III) heme centers bound by an axial $Cys(S^-)$ ligand. TD-DFT calculations, which are unable to fully account for the correlation energy contributions associated with these electronic transitions, provide limited quantitative information; however, we argue that ΔE_1 and ΔE_2 values provide a *comparative* measure of spin−orbit coupling, since these values agree qualitatively with single-point calculations.

Using a tetragonally distorted, strong field d^5 model, we estimated ligand field parameters for a number of hemoproteins with varying axial ligands. This model, introduced by Griffith in the late 1950s and refined through the 1990s, approximates energy differences between the three low-lying, metal-based d_{xy}, d_{xz}, and d_{yz} orbitals from experimentally determined *g*-values.[36,39,42,45,60,61] In low-spin, Fe(III) porphyrins, these orbital energies primarily correspond to Fe 3d-based MOs. The rhombic distortion, V/ξ, approximates the energy difference between d_{xz} and d_{yz}, while the axial distortion, Δ/ξ, approximates the energy difference between d_{xy} and the barycenter of the d_{xz} and d_{yz} (Figure 2). Both rhombic and axial distortions are scaled by the spin−orbit coupling parameter, ξ, which has a value of 464 cm^{-1} for Fe^{3+}.[43] Table 4 summarizes *g*-value assignments and ligand field parameters for hemoproteins bearing a variety of axial ligands, computed using the program developed by McGarvey and Telser.[42,44] By McGarvey's convention, the tetragonal (axial) distortion stabilizes d_{xy} relative to d_{xz}/d_{yz} when $\Delta/\xi < 0$, and the rhombic distortion stabilizes d_{xz} relative to d_{yz} when $V/\xi < 0$.

Ligand field parameters, estimated from experimental *g*-values, validate the computational prediction that thiolate ligation increases the orbital energy separation between Fe $3d_{xy}$-, $3d_{xz}$-, and $3d_{yz}$-based MOs. Magnitudes for rhombic (V, V' in thiolate-ligated porphyrins) and axial (Δ, Δ' in thiolate-ligated porphyrins) splittings increased significantly for hemoproteins bearing an axial $Cys(S^-)$ ligand ($|V'|$ = 1987−2751 cm^{-1} and $|\Delta'|$ = 1960−2765 cm^{-1}) compared to those without a thiolate ligand ($|V|$ = 685−750 cm^{-1} and $|\Delta|$ = 1477−1559 cm^{-1}, Table 4). $Cys(S^-)$ is a charged, strong field ligand that destabilizes d_{xz} and d_{yz} relative to d_{xy}, likely accounting for the increased axial splitting observed in thiolate-ligated porphyrins. Our single-point DFT computations predicted that Fe−S p_π−d_π bonding destabilizes the Fe $3d_{yz}$-based MO relative to the Fe $3d_{xz}$-based MO (Figure 2), an observation that is consistent with a thiolate-dependent increase in rhombic splitting. Furthermore, TD-DFT computations qualitatively recapitulate the thiolate-dependent increase in ground-state/excited-state energy differences that are observed experimentally, although computed ΔE_1 and ΔE_2 values overestimate axial and rhombic splitting parameters by several thousand wavenumbers (Table 3).

The *g*-shifts observed in EPR spectra of low-spin, Fe(III) porphyrins, as well as the resulting ligand field parameters, are sensitive to the identity of the second axial ligand trans to thiolate. Specifically, weaker axial ligands give rise to larger values for $|V'|$ and $|\Delta'|$ (e.g., $|V'|$ = 2751 cm^{-1} and $|\Delta'|$ = 2765 cm^{-1} for cyt $P450_{cam}$ with water trans to thiolate), while stronger axial ligands give rise to smaller values for $|V'|$ and $|\Delta'|$ (e.g., $|V'|$ = 1687 cm^{-1} and $|\Delta'|$ = 2314 cm^{-1} for hCBS with His-based imidazole ring trans to thiolate, Table 4). This trend can be explained in terms of a trans influence; a weaker trans ligand allows for a stronger Fe−S bond and greater thiolate character, giving rise to larger values for $|V'|$ and $|\Delta'|$, as well as smaller *g*-shifts in the rhombic EPR signal. Interestingly, even heme-thiolate proteins bearing identical second axial ligands exhibit different ligand field parameters. For example, hCBS, *Px*RcoM-1, and cyt $P450_{cam}$ + imidazole exhibit axial $Cys(S^-)$/imidazole ligation; however, rhombic and axial splittings differ between these proteins. It is likely that protein-dependent variations to the second coordination sphere (including changes to the thiolate H-bonding environment) give rise to these variations in porphyrin electronic structure.

Our computational data predict that protonation of the coordinating $Cys(S^-)$ in a low-spin, Fe(III) heme leads to diminished spin−orbit coupling and should give rise to a rhombic EPR signal with larger *g*-shifts. We modeled this case by protonating the previously optimized His/$Cys(S^-)$ model and reoptimizing the geometry using DFT. We then compared ground-state bonding and electronic transitions between the His/$Cys(S^-)$ and His/Cys(SH) models in a manner analogous to that described above for other hemoprotein models. Protonation of the coordinating S atom weakens the donor strength of the coordinating cysteine in two ways. First, protonation neutralizes the negative charge and eliminates a strong Coulombic attraction between the metal and ligand (d_{Fe-S} = 2.330 Å for His/Cys(SH) model; d_{Fe-S} = 2.186 Å for His/$Cys(S^-)$ model). Second, as was the case for the His/Met model, there is no Fe−S π-bonding interaction in the His/Cys(SH) model, and the Fe $3d_{yz}$-based MO is stabilized upon

DOI: 10.1021/acs.inorgchem.9b02506
Inorg. Chem. XXXX, XXX, XXX−XXX

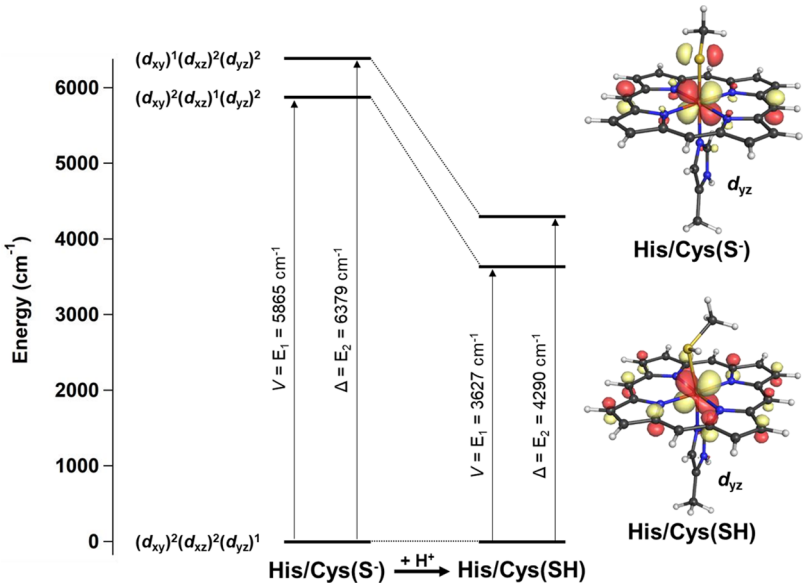

Figure 3. Effects of thiolate protonation on porphyrin electronic structure. Left: Comparison of energy levels between the ground state and two lowest-lying excited states (with corresponding electron configurations shown) in low-spin, Fe(III), d^5 porphyrin models, computed using TD-DFT. Right: Geometry-optimized structures of His/Cys(S^-) and His/Cys(SH) models with an overlay of the Fe $3d_{yz}$-based, spin-down MO. Orbital plots were generated with an isosurface value of 0.05, and structures were visualized using Pymol (v1.3).

Scheme 1. Synthesis of 2-Mercapto-*N*-phenylbenzamides Derivatives from 2,2′-Disulfanediyldibenzoyl Chloride[a]

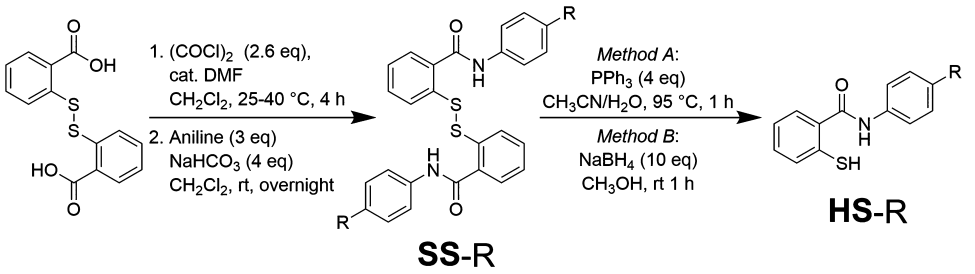

[a]R = CH_3, H, Cl, CF_3, and NO_2. Disulfides are abbreviated as "**SS**-R" and aryl thiols are abbreviated as "**HS**-R".

protonation (Figure S6). Consequently, values for ΔE_1 and ΔE_2 are reduced by ~2000 cm^{-1} (Figure 3). A stabilized Fe $3d_{yz}$-based MO and smaller values for ΔE_1 and ΔE_2 reflect greater spin−orbit coupling, which should give rise to larger magnitude *g*-shifts. H-bonding represents an intermediate case between a fully deprotonated thiolate and a protonated thiol; therefore, we hypothesize that the dispersion of *g*-values in the rhombic, low-spin EPR signal observed for a six-coordinate, Fe(III) heme-thiolate protein should reflect the strength of the thiolate H-bonding network.

3.2. Synthesis of Intramolecularly Hydrogen-Bonded Aryl Thiolate Ligands. To test our hypothesis that EPR spectroscopy may be sensitive to changes in the H-bonding environment in heme-thiolate proteins, we utilized a series of aryl thiolate ligands in which the strength of an intramolecular hydrogen bond (H-bond) to the Fe-coordinating thiolate may be systematically tuned. Our chosen ligand set takes inspiration from the substituted 2-acylaminobenzenethiolate ligands reported by Ueyama et al.,[62] whose syntheses we have been unable to successfully reproduce. The newly utilized ligand series contains a 2-mercaptobenzamide core, in which an intramolecular N−H···S H-bond exists between the amide and coordinating aryl thiolate S atom. This intramolecular H-bond results in the formation of a six-membered ring, an improvement over the originally employed ligand in which a five-membered ring was formed. Expansion of the ring by one atom allows the D−H···A angle to further approach 180°, the ideal angle for this H-bonding interaction. To systematically tune the strength of the intramolecular H-bond, we varied the electronics of the amide by changing the identity of an *N*-phenyl para substituent. We chose this para substitution strategy for three reasons. First, the effects of para substituent electron-donating/-withdrawing properties on the pK_a of a heteroatom proton are well-characterized and concisely encompassed in the Hammett parameter, σ.[63] We anticipate para substituents with a more positive σ value will lower the pK_a of the amide proton and result in a stronger H-bond and vice versa. Second, by making substitutions at the amide phenyl ring, we avoid substantially influencing the thiolate donor strength directly, and instead isolate the effects of changes in H-bond strength. Finally, synthesis of these compounds relies on a facile two-step syntheses from an acyl chloride and commercially available, para-substituted aniline derivatives.[64,65]

We successfully synthesized five 2-mercapto-*N*-phenylbenzamide derivatives (**HS**-R, R = CH_3, H, Cl, CF_3, NO_2), which serve as intramolecularly H-bonded thiolate ligand precursors, using a two-step synthetic method (Scheme 1). We

DOI: 10.1021/acs.inorgchem.9b02506
Inorg. Chem. XXXX, XXX, XXX−XXX

Table 5. Comparison of the NMR Chemical Shifts (ppm) of the 5-c Aryl Thiolate Porphyrin Complexes, [Fe(TPP)(S-R)][a]

R	β-pyrrole	m-Ph, TPP	o-Ph, TPP	p-Ph, TPP	m-Ph, SPh's	o-Ph, SPh	p-Ph, SPh	o/m-PhL−H	p-PhL−H
CH_3	72.5	12.8	9.6	6.9	64.3, 56.6	−93.0	−85.6	−110.7, 8.4, 4.8	4.1
H	71.6	12.8	9.8	6.9	63.7, 56.4	−92.8	−85.3	−111.3, 8.3, 4.9	6.5
Cl	71.5	12.8	9.6	6.8	62.5, 55.6	−91.9	−84.5	−111.6, 8.3, 4.8	
CF_3	68.4	12.8	9.9	6.9	61.2, 54.8	−90.4	−83.2	−110.5, 8.0, 5.1	
NO_2	70.5	12.9	10.5	6.7	59.9, 54.3	−90.2	−82.7	−112.4, 8.2, 4.9	

[a]R refers to the identity of the *N*-phenyl para substituent, recorded in CD_2Cl_2 at room temperature (between 20 and 22 °C).

reacted 2,2′-disulfanediyldibenzoyl chloride with five different commercially available, para-substituted anilines under basic conditions to generate 2,2′-disulfanediylbis(*N*-phenylbenzamide) derivatives with varying *N*-phenyl para substitution (**SS**-R, R = CH_3, H, Cl, CF_3, NO_2, Figures S7−S17). Strategically, we chose to carry out the amide formation reaction using these disulfides in order to eliminate side-reactions between the thiol moiety and acyl chloride intermediate. Reduction of the 2,2′-disulfanediylbis(*N*-phenylbenzamide) disulfide bond using either triphenylphosphine or sodium borohydride, followed by protonation of the charged thiolate, resulted in formation of our desired thiol ligand precursors (Figures S18−S28). In ^{1}H NMR spectra of the thiols, we observed a direct correlation between the chemical shift observed for the amide proton and electron-withdrawing strength of the *N*-phenyl para substituent, as represented by the two extremes: δ_{N-H} (**HS**-CH_3) = 7.65 ppm and δ_{N-H} (**HS**-NO_2) = 8.18 ppm. No such correlation was observed for protons in the aryl thiol ring. Taken together, these observations serve as preliminary evidence of a localized, systematic change in the electronic properties of the amide proton. The nature of this systematic change in electronics is enumerated below.

3.3. Preparation of Five-Coordinate, Fe(III) Thiolate-Ligated Porphyrins. We prepared a series of five complexes of the form [Fe(TPP)(**S**-R)] using the intramolecularly H-bonded thiol ligand precursors, **HS**-R (R = CH_3, H, Cl, CF_3, NO_2). We assembled each complex using the procedure recently reported by Hunt and Lehnert for the synthesis of 5-c, Fe(III) tetraphenylporphyrinate complexes bearing an axial aryl thiolate ligand.[10] This method involves mixing [Fe(TPP)-(OCH_3)] with a slight excess of thiol ligand precursor in dry CH_2Cl_2. The strongly basic methoxide ligand deprotonates the aryl thiol, resulting in coordination of the aryl thiolate and formation of 1 equiv of methanol. We used electronic absorption spectroscopy to monitor the reaction, which typically progresses to completion within 1 min. Characteristic spectroscopic features of each [Fe(TPP)(**S**-R)] complex include a split Soret peak with a shoulder at 380 nm and maximum at 407−408 nm, in addition to other peaks at 515, 576−578, and 717−722 nm (Figures S30, S33, S36, S39, and S43).

Each recrystallized [Fe(TPP)(**S**-R)] compound was characterized using EPR and ^{1}H NMR spectroscopies and exhibited distinct features indicative of a high-spin, Fe(III) porphyrin complex. Effective *g*-values were observed at *g* = 7.1, 4.8, and 1.9 in the EPR spectrum of each compound, suggesting the presence of a high-spin (*S* = 5/2), rhombic paramagnetic species (Figures S31, S34, S37, S40, and S44). An additional sharp signal around *g* = 6.0 was observed in all EPR spectra, derived from a very small amount of [Fe(TPP)Cl] impurity (Figure S29). Assignment of ^{1}H NMR chemical shifts are summarized in Table 5 and Scheme 2. These chemical shift assignments draw on those made for other [Fe(TPP)]$^+$ complexes bound to aryl thiolate ligands.[10] Importantly, peaks for β-pyrrole protons were observed between 68.4 and 72.5 ppm, a range that is characteristic of paramagnetic shifts due to the presence of a high-spin, Fe(III) porphyrin species (Figures S32, S35, S38, S41, and S45). We observed a correlation between the identity of the *N*-phenyl para substituent and the magnitude of the chemical shift observed for protons in the ortho, meta, and para positions of the coordinating aryl-thiolate: as the electron-withdrawing character of the *N*-phenyl para substituent increases, giving rise to a stronger intramolecular H-bond, the magnitude of the paramagnetic shift decreases. Considering that a stronger H-bond gives rise to a weaker Fe−S bond (*vide infra*), attenuation of the interaction between the paramagnetic, high-spin (*S* = 5/2) Fe(III) center and the ligand-derived protons may cause the observed trends in paramagnetic shifts; however, in-depth analysis of the observed paramagnetic shifts would be required to fully substantiate this hypothesis.

Scheme 2. Labeling Scheme for the Observed Signals in the ^{1}H NMR Spectra Reported in Table 5

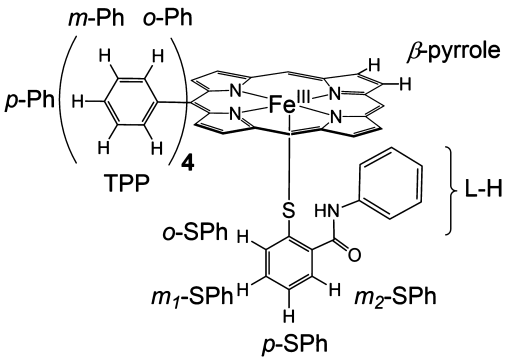

The crystal structure of [Fe(TPP)(**S**-NO_2)] revealed an intramolecular H-bonding interaction between the ligand amide and Fe-coordinated thiolate (Figure 4). Geometric parameters for [Fe(TPP)(**S**-NO_2)] (Fe−S bond distance, Fe−S = 2.3078(8) Å, average Fe−N bond distance, Fe−N_{av} = 2.064(5) Å, and Fe atom displacement from the mean plane of the coordinating N atoms, Fe atom displacement = 0.4181(8) Å) are comparable to those reported for [Fe(TPP)(SPh)] by Byrn and Strouse (Fe−S = 2.315(2) Å, Fe−N_{av} = 2.063 Å, Fe atom displacement = 0.470(1) Å)[66] and are therefore consistent with aryl-thiolate coordination. The conformation of the amide relative to the coordinating S atom is consistent with the presence of an intramolecular interaction in which the amide acts as an H-bond donor to the coordinating S atom. A donor−acceptor distance of 3.0087(19) Å and a D−H···A angle of 149(2)° are indicative of a weak H-bonding interaction. The contribution of this intramolecular H-bond to the attenuation of thiolate ligand strength is supported by spectroscopic and computational results detailed below.

DOI: 10.1021/acs.inorgchem.9b02506
Inorg. Chem. XXXX, XXX, XXX−XXX

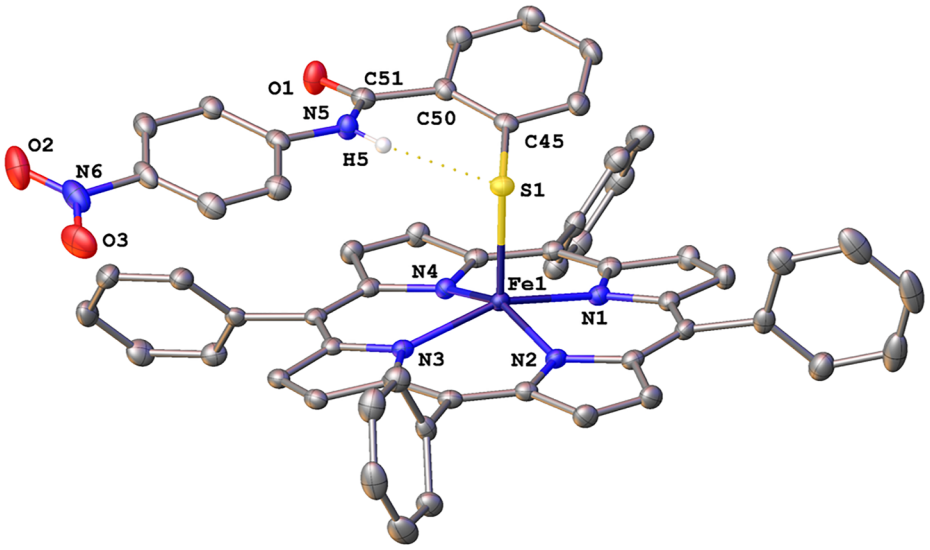

Figure 4. Molecular structure of [Fe(TPP)(**S**-NO2)] shown with 50% probability ellipsoids and selected atom IDs. The amide H atom is displayed, and all other H atoms are omitted for clarity. The yellow dots denote the intramolecular H-bond between the amide proton and coordinating S atom.

3.4. Assembly and EPR Spectroscopic Characterization of Six-Coordinate, Fe(III) Thiolate-Ligated Porphyrins. By mixing each of the five-coordinate [Fe(TPP)(**S**-R)] complexes with a neutral donor ligand, we successfully assembled six-coordinate model complexes that exhibit EPR spectra characteristic of low-spin, Fe(III) thiolate-ligated porphyrins. We utilized two biologically relevant neutral donor ligands to mimic heme-thiolate protein environments: 1-methylimidazole (1-MeIm), which gives rise to axial ligation similar to the Cys/His environment observed in Fe(III) hCBS and RcoM, and water, which gives rise to axial ligation similar to the Cys/H_2O environment observed in Fe(III), substrate-free cytochromes P450. Upon addition of 1-MeIm (liquid) to a solution of each five-coordinate complex (in 50:50 CH_2Cl_2/toluene), we observe an EPR signal characteristic of a low-spin, Fe(III) thiolate-ligated porphyrin complex (g_z = 2.479−2.491, g_y = 2.280−2.283, and g_x = 1.868−1.877), which we attribute to the six-coordinate [Fe(TPP)(**S**-R)(1-MeIm)] complexes (Figure S46). We also observe a very minor high-spin (S = 5/2) signal (less than 1% total signal intensity) with $g_\perp$ = 5.9 and $g_\parallel$ = 2.0 for each complex, which we attribute to a small [Fe(TPP)Cl] contaminant (Figure S46). We were unable to observe formation of [Fe(TPP)(**S**-R)(OH_2)] complexes when adding exogenous water to a solution of five-coordinate complex due to the immiscibility between water and the 50:50 CH_2Cl_2/toluene solvent. To overcome this limitation, we prepared EPR samples using solvent that was not rigorously dried by distillation over CaH_2. Potentiometric titration using an automated Karl Fischer titrator revealed that this "wet" 50:50 CH_2Cl_2/toluene mixture contained a concentration of water greater than 2 mM. Upon dissolution of each five-coordinate porphyrin model complex to a concentration of ∼500 μM in wet solvent, we observe an EPR signal characteristic of a low-spin, Fe(III) thiolate-ligated porphyrin complex which is distinct from that observed in the presence of 1-MeIm. This new signal, which we attribute to a six-coordinate [Fe(TPP)(**S**-R)(OH_2)] complex (g_z = 2.416−2.429, g_y = 2.267−2.272, and g_x = 1.912−1.917), is less anisotropic than the signal observed for the 1-MeIm-bound complexes (Figure S46). The minor [Fe(TPP)Cl] contaminant is also observed for the water-bound complexes. We observed a similar rhombic, low-spin signal upon addition of dry methanol to 5-c [Fe(TPP)(**S**-R)] complexes (data not shown). A representative overlay of low-spin, Fe(III) EPR spectra for both six-coordinate [Fe(TPP)(**S**-CH_3)(L′)] complexes is displayed in Figure 5.

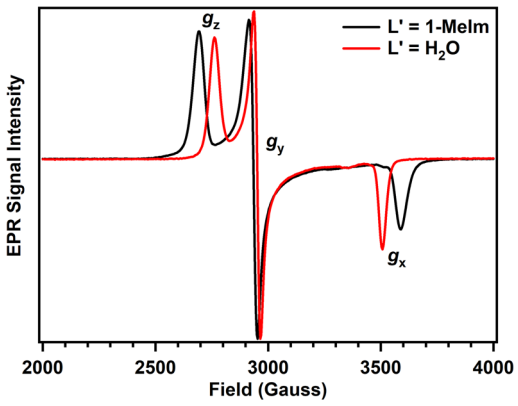

Figure 5. Overlay of low-spin, Fe(III) EPR signals observed for six-coordinate [Fe(TPP)(**S**-CH_3)(L′)] complexes where L′ = 1-MeIm (black) or H_2O (red). Samples were dissolved in 50:50 CH_2Cl_2/toluene, and spectra were recorded at 10 K. Signal intensities are normalized to the most intense feature at g_y.

A positive correlation exists between g-value dispersion and intramolecular H-bond strength for six-coordinate [Fe(TPP)(**S**-R)(L′)] complexes. Figure 6 compares the low-spin, Fe(III) EPR signals observed for six-coordinate complexes with either 1-MeIm or water bound as the sixth axial ligand trans to the aryl thiolate. A clear trend is apparent in both sets of complexes: the g-value dispersion of the low-spin, rhombic EPR signal increases as the electron-withdrawing character of the amide N-phenyl para substituent increases. As described above, the electron-donating/-withdrawing character of this substituent tunes the acidity of the amide proton and thereby modulates the strength of the N−H···S hydrogen bond *without* significantly altering the electronics of the thiophenolate ring

DOI: 10.1021/acs.inorgchem.9b02506
Inorg. Chem. XXXX, XXX, XXX−XXX

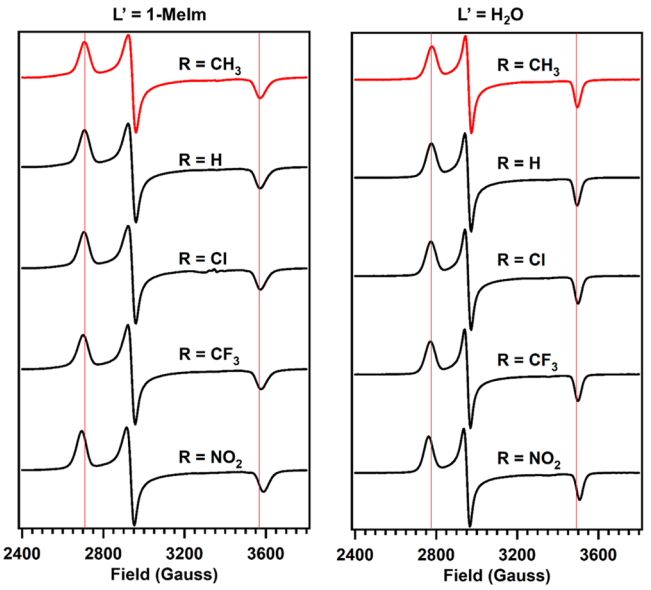

Figure 6. Comparison of rhombic, low-spin spectra observed for six-coordinate [Fe(TPP)(**S**-R)(L′)] complexes where L′ = 1-MeIm (left) or H_2O (right). Samples were prepared in 50:50 CH_2Cl_2/toluene, and spectra were recorded at 10 K. Signal intensities are normalized to the most intense feature at g_y. The vertical lines, centered on g_z and g_x for [Fe(TPP)(**S**-Cl)(L′)] (red), help depict changes in *g*-value dispersion as the electron-withdrawing character of the amide para substituent (R) increases.

directly. We therefore conclude that the observed trend is indicative of a direct correlation between intramolecular N−H···S hydrogen bond strength and low-spin, Fe(III) EPR signal *g*-value dispersion (Table 6). The connection of these trends to the porphyrin electronic structure are discussed in detail below.

Table 6. EPR Parameters for [Fe(TPP)(S-R)(L′)] Complexes[a]

R	L′ = 1-MeIm			L′ = H_2O		
	g_z	g_y	g_x	g_z	g_y	g_x
CH_3	2.479	2.280	1.877	2.416	2.267	1.917
H	2.478	2.279	1.877	2.417	2.268	1.919
Cl	2.481	2.280	1.875	2.419	2.268	1.916
CF_3	2.484	2.281	1.874	2.421	2.270	1.916
NO_2	2.491	2.283	1.868	2.429	2.272	1.912

[a] g_z, g_y, and g_x are given the historical assignments of g_{max}, g_{mid}, and g_{min} in this table to facilitate comparison of *g*-values to those of heme-thiolate proteins reported in the literature.

3.5. Computationally-Observed Changes in Thiolate H-Bonding. We generated geometry-optimized models of six-coordinate [Fe(TPP)(**S**-R)(L′)] (L′ = 1-MeIm, H_2O) complexes using DFT calculations (BP86, TZVP). To generate initial coordinates for each model, we used the crystal structure of five-coordinate [Fe(TPP)(**S**-NO_2)]. We modified these atomic coordinates to reflect the appropriate para substitution and added a second axial ligand, either 1-MeIm or H_2O. Additionally, we employed porphinate (P^{2-}) as a simplified porphyrin structure by replacing each of the tetraphenylporphyrin *meso* phenyl rings with a hydrogen atom. Frequency calculations ensured that each geometry-optimized model represents an energy minimum, as reflected by the lack of any computed negative vibrational frequencies. Representative geometry-optimized structures for both [Fe(P)(**S**-NO_2)(L′)] models are displayed in Figure 7.

Computed geometric parameters and vibrational frequencies for [Fe(P)(**S**-R)(L′)] models support our hypothesis that the electron-donating or -withdrawing character of each *N*-phenyl para substituent directly correlates with the strength of the intramolecular N−H···S hydrogen bond. Increasing the electron-withdrawing strength of the para substituent resulted in a marked decrease in calculated amide N−H vibrational frequency, as well as a slight lengthening of the N−H bond (Table 7). These observations suggest that changing the identity of the para substituent modulates the amide N−H bond strength, and by extension, the acidity of the amide proton. For example, in [Fe(P)(**S**-R)(1-MeIm)] models, the electron-donating methyl substituent gave rise to a *stronger* N−H bond (ν_{N-H} = 3258 cm^{-1}) and a *less acidic* amide proton, as compared to the strongly electron-withdrawing nitro substituent, which gave rise to a significantly *weaker* N−H bond (ν_{N-H} = 3176 cm^{-1}) and a *more acidic* amide proton. Amide proton acidity, approximated by N−H bond strength, directly influences the strength of the intramolecular N−H···S hydrogen bond: As the amide N−H bond is weakened, the H-bond donor−acceptor distance decreases, as does the distance between the amide H atom and thiolate S atom (Table 7). For example, the [Fe(P)(**S**-NO_2)(1-MeIm)] model, which exhibited the weakest amide N−H bond, possessed the strongest H-bond, represented by the shortest donor−acceptor distance (3.050 Å). The same trends are observed in to a similar degree in [Fe(P)(**S**-R)(H_2O)] models.

Computations predict that strengthening the intramolecular N−H···S hydrogen bond results in a weakening of the Fe−S bond. We observed a small but consistent increase in Fe−S bond distance as the electron-withdrawing character of the para substituent (and H-bond strength) increased, ranging from 2.234 Å in [Fe(P)(**S**-CH_3)(1-MeIm)] to 2.245 Å in [Fe(P)(**S**-NO_2)(1-MeIm)] (Table 7). We also observed this trend in the water-bound series, where the Fe−S bond lengths ranged from 2.192 Å in [Fe(P)(**S**-CH_3)(H_2O)] to 2.198 Å in [Fe(P)(**S**-NO_2)(H_2O)]. Weakening of the Fe−S bond results in a concomitant strengthening of the bond between iron and the sixth axial ligand: The Fe−N(1-MeIm) bond shortens from 2.076 Å in [Fe(P)(**S**-CH_3)(1-MeIm)] to 2.070 Å in [Fe(P)(**S**-NO2)(1-MeIm)], while the Fe−O bond shortens from 2.215 Å in [Fe(P)(**S**-CH_3)(H_2O)] to 2.207 Å in [Fe(P)(**S**-NO_2)(H_2O)]. Using DFT, Paulat et al. predicted a similar direct correlation between intramolecular H-bond strength and Fe−S bond distance for a series of porphyrin-thiolate model compounds with zero, one, or two intramolecular H-bonds.[67] The electronic origins of the observed changes in bonding of axial porphyrin ligands will be discussed below.

3.6. Insight into H-Bond-Dependent Changes in Model Porphyrin-Thiolate Electronic Structure. Rhombic and axial splittings decreased as intramolecular H-bond strength increased in our 6-c porphyrin-thiolate models. Using the tetragonally distorted, strong field d^5 model described above, we estimated ligand field parameters for these compounds from experimentally observed *g*-values. (Table 8). For both sets of [Fe(TPP)(**S**-R)(L′)] compounds, we observe a small *decrease* in rhombic and axial splittings as H-bond strength *increases* (for L′ = 1-MeIm, $\Delta|V'|$ = 115 cm^{-1}, $\Delta|\Delta'|$ = 82 cm^{-1}; for L′ = H_2O, $\Delta|V'|$ = 77 cm^{-1}, $\Delta|\Delta'|$ = 61 cm^{-1}). This observation demonstrates that the intramolecular

DOI: 10.1021/acs.inorgchem.9b02506
Inorg. Chem. XXXX, XXX, XXX−XXX

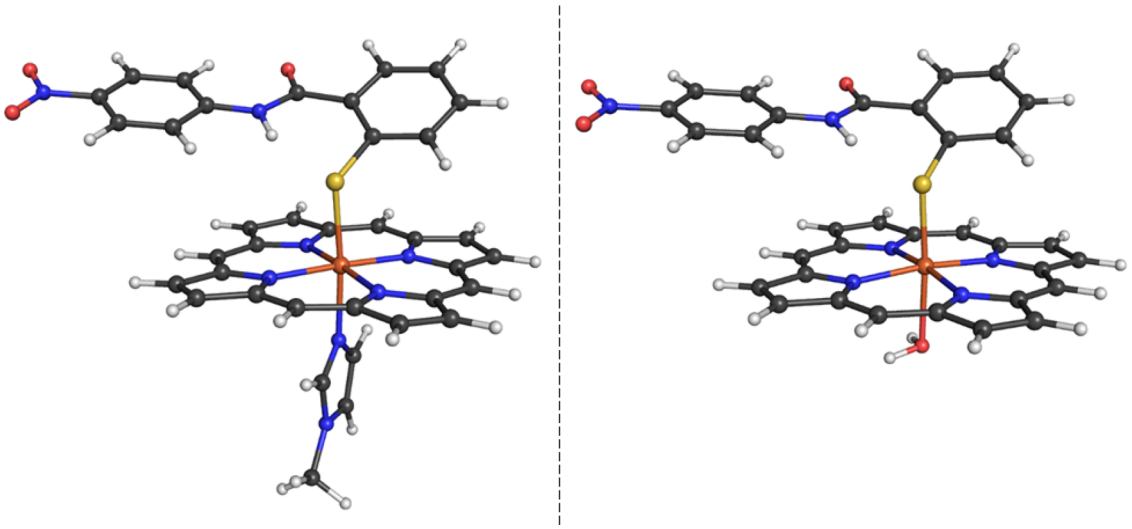

Figure 7. DFT-optimized structures of [Fe(P)(S-NO_2)(L′)] complexes with L′ = 1-MeIm (left) and L′ = H_2O (right). Structures were visualized using Pymol (v1.3).

Table 7. Geometric Parameters and Amide N−H Vibrational Frequencies for [Fe(TPP)(S-R)(L′)] Complexes Computed Using DFT

	L′ = 1-MeIm						L′ = H_2O					
R	ν_{N-H} (cm^{-1})	d_{N-H} (Å)	d_{D-A} (Å)	$d_{S-H(amide)}$ (Å)	d_{Fe-S} (Å)	$d_{Fe-N(ax)}$ (Å)	ν_{N-H} (cm^{-1})	d_{N-H} (Å)	d_{D-A} (Å)	$d_{S-H(amide)}$ (Å)	d_{Fe-S} (Å)	d_{Fe-O} (Å)
CH_3	3258	1.032	3.070	2.162	2.234	2.076	3306	1.029	3.089	2.198	2.192	2.215
H	3252	1.032	3.068	2.159	2.237	2.073	3301	1.030	3.087	2.193	2.194	2.212
Cl	3230	1.034	3.061	2.145	2.239	2.071	3279	1.031	3.079	2.178	2.195	2.211
CF_3	3214	1.034	3.059	2.142	2.243	2.071	3266	1.032	3.075	2.171	2.197	2.207
NO_2	3176	1.036	3.050	2.124	2.245	2.070	3234	1.034	3.067	2.155	2.198	2.207

Table 8. Ligand Field Parameters Computed from Experimental *g*-Values for [Fe(TPP)(S-R)(L′)] Compounds

L′	R	g_x	g_y	g_z	V'/ξ^a	$\lvert V\rvert$ (cm^{-1})	Δ'/ξ^b	$\lvert\Delta\rvert$ (cm^{-1})	k^c	V'/Δ'^d
1-MeIm	CH_3	−2.479	−2.280	1.877	−4.380	2015	−4.665	2146	1.068	0.939
	H	−2.478	−2.279	1.877	−4.377	2013	−4.668	2147	1.065	0.938
	Cl	−2.481	−2.280	1.875	−4.339	1996	−4.637	2133	1.063	0.936
	CF_3	−2.484	−2.281	1.874	−4.320	1987	−4.631	2130	1.065	0.933
	NO_2	−2.491	−2.283	1.868	−4.213	1938	−4.535	2086	1.056	0.929
H_2O	CH_3	−2.416	−2.267	1.917	−5.486	2524	−5.354	2463	1.147	1.025
	H	−2.417	−2.268	1.919	−5.564	2559	−5.436	2501	1.165	1.024
	Cl	−2.419	−2.268	1.916	−5.449	2507	−5.340	2456	1.148	1.020
	CF_3	−2.421	−2.270	1.916	−5.459	2511	−5.335	2454	1.155	1.023
	NO_2	−2.429	−2.272	1.912	−5.314	2444	−5.257	2418	1.147	1.011

[a] V'/ξ = rhombic splitting, ξ = 460 cm^{-1}. [b] Δ'/ξ = axial splitting. [c] k = orbital reduction factor. [d] V'/Δ' = rhombicity.

H-bond attenuates the thiolate ligand strength, ultimately giving rise to smaller *g*-shifts in the rhombic, low-spin EPR signal. The *trans* influence observed in heme-thiolate proteins was also observed in our porphyrin-thiolate models: Rhombic and axial splittings were larger for the water-bound complexes than for 1-MeIm-bound complexes.

As was the case for hemoprotein models with variable axial ligands, we can rationalize the *g*-shift variations observed in our H-bonding models in terms of Fe−S bonding interactions. H-bond donation to the coordinating thiolate (much like protonation of the thiolate) alters Fe−S bonding in two ways. First, H-bonding effectively reduces the negative charge on sulfur and thereby reduces the ligand donor strength. Second, the H-bond diminishes the Fe−S π-bonding interaction, as evidenced by a decrease in sulfur 3p character observed in the Fe-based $3d_{yz}$ MOs of H-bonding models (Figure S47). Increasing the strength of the H-bond enhances these two effects and leads to a weakening of the Fe−S bond, as evidenced by the correlation between H-bond strength and Fe−S bond distance observed in computational models of our complexes (Table 7). Weakening of the Fe−S bond causes a reduction in the π^*-antibonding character and subsequent stabilization of the singly occupied Fe $3d_{yz}$-based MO. Stabilization of d_{yz} brings the lowest-lying Kramers doublets closer together in energy, giving rise to enhanced spin−orbit coupling and larger magnitude *g*-shifts in the presence of a stronger H-bond. TD-DFT-computed transition energies for [Fe(P)(S-R)(H_2O)] models provide additional evidence that H-bonding enhances spin−orbit coupling (Table 9). Values for both ΔE_1 and ΔE_2 fell between those computed for the His/

DOI: 10.1021/acs.inorgchem.9b02506
Inorg. Chem. XXXX, XXX, XXX−XXX

Table 9. Electronic Excitation Energies for [Fe(P)(S-R)(H_2O)] Computed Using TD-DFT

R	E_1 (cm^{-1})	E_2 (cm^{-1})
CH_3	5442	5812
H	5428	5791
Cl	5388	5756
CF_3	5374	5724
NO_2	5337	5687

Cys(S^-) and His/Cys(SH) models, consistent with the fact that H-bonding represents an intermediate protonation state. We observed a decrease in values for ΔE_1 and ΔE_2 of approximately 100 cm^{-1} when comparing values between [Fe(P)(S-CH_3)(H_2O)], which contains the weakest H-bond, and [Fe(P)(S-NO_2)(H_2O)], which contains the strongest H-bond. As was the case with the hemoprotein models above, we caution against interpreting TD-DFT data in a quantitative fashion (ΔE_1 and ΔE_2 largely overestimate V' and Δ'); however, the trends observed in TD-DFT computations support the hypothesis that H-bond donation to thiolate leads to enhanced spin−orbit coupling.

4. DISCUSSION

We have uncovered the electronic origins of the unique rhombic EPR signal observed in low-spin, Fe(III) heme-thiolate proteins. Our DFT computations revealed a π-bonding interaction between Fe and S that is unique to porphyrins bearing an axial thiolate ligand. This $p_\pi-d_\pi$ interaction destabilizes the singly occupied, Fe $3d_{yz}$-based MO and gives rise to larger energy differences between the ground state and two lowest-lying excited states. These large ground-/excited-state energy differences, predicted using TD-DFT, reflect diminished spin−orbit coupling between the ground-state Kramers doublet and two low-lying excited states. Diminished spin−orbit coupling ultimately gives rise to the reduced magnitude of g-shifts observed for heme-thiolate proteins. Ligand field parameters for low-spin, Fe(III) porphyrins, estimated from experimentally observed g-values, corroborate our computational results: We observed significantly larger rhombic and axial splittings in hemoproteins bearing an axial thiolate ligand compared to hemoproteins with no axial thiolate.

We visualized the unique features of the heme-thiolate electronic structure by plotting rhombic and axial splittings for a number of low-spin, Fe(III) hemoproteins bearing different axial ligands (Figure 8A). The resulting correlation diagram resembles that originally developed by Blumberg and Peisach in the 1970s;[68] however, our new correlation diagram utilizes McGarvey's systematic approach for identifying the proper g-tensor axis system for each species.[42] As is the case in the Blumberg−Peisach diagram, porphyrin species in Figure 8A cluster based on the identity of the two axial heme ligands. Species bearing neutral donors (i.e., His/Met- and His/His-ligated porphyrins) exhibit the lowest magnitude values for rhombic and axial splittings. His/His(N^-)-bound porphyrins exhibit slightly larger splittings than neutral His/His-bound species, and hydroxide/phenoxide-bound porphyrins exhibited large rhombic splitting. As detailed above, thiolate-bound porphyrins exhibit the largest values for axial splitting and moderate-to-large rhombic splitting. Within the broad group of thiolate-ligated porphyrins, two distinct clusters emerge based on the identity of the second axial ligand, reflecting the neutral donor trans influence.

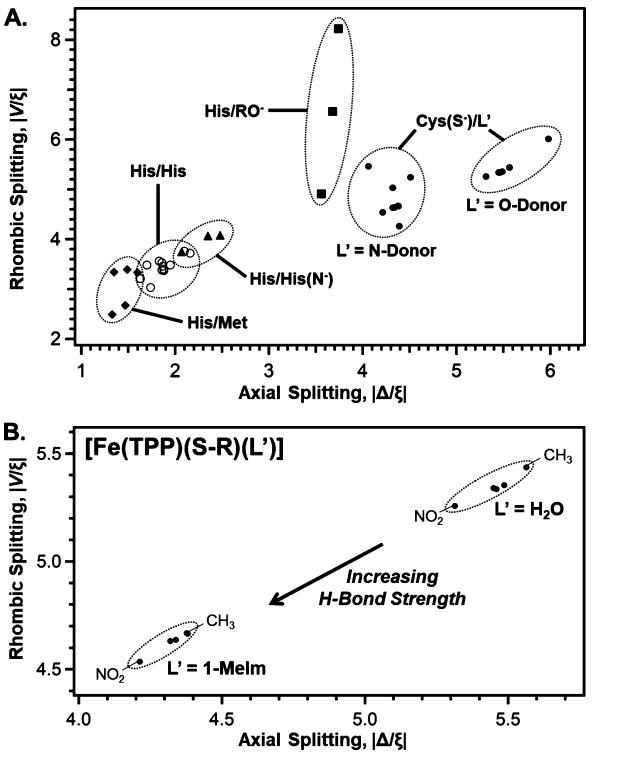

Figure 8. (A) Rhombic versus axial splitting correlation diagram for low-spin, Fe(III) hemoproteins and porphyrin complexes computed from experimentally derived g-values. EPR parameters utilized to create the correlation diagram were obtained in this study or from literature values.[4,28,30,33−36,69] Porphyrin species are grouped according to the identity of the two axial heme ligands. (B) Relationship between rhombic splitting, axial splitting, and H-bond strength in [Fe(P)(S-R)(L')] complexes. For both sets of complexes, the magnitude of rhombic and axial splittings decreases as H-bond strength increases.

Through synthesis and characterization of porphyrin-thiolate model compounds bearing a tunable, intramolecular H-bond, we have established a direct correlation between the magnitude of g-shifts observed in the rhombic EPR signal of low-spin, Fe(III) heme-thiolates and thiolate H-bond strength. To model H-bonding in heme-thiolates, we utilized a thiolate ligand with an intramolecular N−H···S H-bond between an amide and aryl thiolate S atom, and we systematically tuned the strength of this H-bond by varying the electronics of the amide. Spectroscopic investigation of low-spin, Fe(III) porphyrin complexes bearing our model thiolates (in addition to a second axial ligand, water, or 1-methylimidazole) revealed a direct correlation between H-bond strength and g-shift in the rhombic EPR signal. Axial and rhombic splittings, computed from experimental g-values, also correlate with H-bond strength. Interestingly, changes in thiolate H-bond strength give rise to the same slope on the correlation diagram in compounds with water or 1-methlyimidazole bound as the trans ligand (Figure 8B). This observation demonstrates that for heme-thiolates with a single H-bond and a fixed geometry the thiolate H-bond donor strength influences heme electronic structure in a similar manner irrespective of sixth axial ligand identity. By elucidating this relationship between H-bond strength and heme-thiolate electronic structure, we provide a

DOI: 10.1021/acs.inorgchem.9b02506
Inorg. Chem. XXXX, XXX, XXX−XXX

new means to assess the H-bonding environment of heme-thiolate proteins using the correlation diagram.

We employed DFT computations to better understand this correlation in terms of heme-thiolate electronic structure. From DFT, we observe that H-bonding attenuates the Fe−S π-bonding interaction and thereby stabilizes the Fe $3d_{yz}$-based MO. An important consequence of this stabilization is to decrease ground-/excited-state energy differences, and TD-DFT predicts a *systematic decrease* in these energy differences as H-bond strength *increases* in [Fe(P)(S-R)(H_2O)] compounds. These computational observations suggest that H-bonding gives rise to greater spin−orbit coupling through reduction in ground-/excited-state energy differences, as well as through decreased Fe−S covalency. Spin−orbit coupling directly contributes to the magnitude of the EPR *g*-shift; thus, an *increase* in heme-thiolate H-bond strength leads to an *increase* in the magnitude of *g*-shifts.

Given the well-defined relationship between heme-thiolate electronic structure and rhombic EPR signal, it is possible to compare thiolate donor strengths among heme-thiolate proteins through analysis of low-spin, Fe(III) EPR spectra. As an example, we compare the EPR signals (and resulting ligand field parameters) observed in imidazole-bound Fe(III) Cyt $P450_{cam}$, a type-1 heme-thiolate protein, with that of *Px*RcoM-1, a type-2 heme-thiolate protein (Table 4). These hemoproteins bear axial ligands that are nearly identical. However, rhombic splitting is slightly larger in *Px*RcoM-1 ($|V'|$ = 2019 cm^{-1}) than in Cyt $P450_{cam}$ ($|V'|$ = 1868 cm^{-1}), while axial splitting is significantly larger in Cyt $P450_{cam}$ ($|\Delta'|$ = 2512 cm^{-1}) than in *Px*RcoM-1 ($|\Delta'|$ = 1960 cm^{-1}). Slightly larger rhombic splitting in *Px*RcoM-1 suggests that the heme in this protein possesses slightly greater Fe−S p_π−d_π bonding character than in Cyt $P450_{cam}$. In contrast, the significantly *smaller* axial splitting in *Px*RcoM-1 suggests that the thiolate in this protein is a weaker donor than the thiolate in Cyt $P450_{cam}$. These differences in heme-thiolate electronic structure are consistent with each protein's function. Cyt $P450_{cam}$ is a monooxygenase enzyme that requires a strong thiolate donor ligand to facilitate O−O bond cleavage and increase the basicity of the protonated ferryl species in compound II.[2,3,10,22−26] In *Px*RcoM-1, the thiolate ligand is replaced by a protein-derived methionine ligand upon heme reduction,[27,28] which may explain why the heme-coordinating thiolate is a weaker donor than that in Cyt $P450_{cam}$.

It is likely that second coordination sphere interactions, such as H-bonding, impart differential thiolate donor strengths in heme-thiolate proteins. The crystal structure of Cyt $P450_{cam}$ reveals a well-defined thiolate H-bonding network that includes three backbone amide H-bond donors.[15] Long donor−acceptor distances (3.08−3.56 Å) and nonlinear D−H−A angles (88−126°) demonstrate that H-bonding to thiolate is relatively weak in this protein. Our EPR analysis, which points to a relatively strong thiolate donor in Cyt $P450_{cam}$, is consistent with a weak thiolate H-bonding network. While no structural data exist for *Px*RcoM-1, it is likely that the second coordination sphere differs significantly from that of Cyt $P450_{cam}$. Analysis of the *Px*RcoM-1 rhombic EPR signal suggests that the overall thiolate donor strength is weaker than that of Cyt $P450_{cam}$. We speculate that a strong H-bond may exist between the coordinating thiolate and a protein-derived H-bond donor in *Px*RcoM-1. This strong H-bond would facilitate redox-mediated ligand switching by weakening the Fe−S bond.

The intramolecularly H-bonded porphyrin complexes characterized in this study offer a new way to model the thiolate H-bonding network and its role in tuning the reactivity of heme-thiolate proteins. Hunt and Lehnert recently shed light on the electronic nature of the "thiolate push" effect, which gives rise to O−O bond cleavage in Cyt P450s, in terms of an admixture of Fe−S σ-bonding and Fe−O−O σ^*-antibonding in a doubly protonated model of the Compound 0 ferric peroxo species.[10] This study demonstrated that modulating the thiolate donor strength influences this critical bonding interaction, and the authors hypothesize that H-bonding provides a means to attenuate thiolate donor strength. Our current study lends support to this hypothesis. Through computational and spectroscopic analysis of a model system in which we systematically tune the strength of a heme-thiolate H-bonding interaction, we have identified a clear connection between H-bonding and thiolate ligand strength. On the basis of changes in the magnitude of *g*-shifts in low-spin, rhombic EPR spectra, we demonstrate that increasing the strength of H-bonding to thiolate leads to a decrease in thiolate donor strength. The functional implications of these changes in H-bonding in our model system have yet to be explored.

In conclusion, we developed a synthetic model of H-bonding in heme-thiolate proteins in which the strength of an intramolecular H-bond may be finely tuned. We utilized this model system to demonstrate that H-bond donation to thiolate influences the Fe−S bonding interaction in heme-thiolates using a combination of computational methods and EPR spectroscopy. We defined a direct correlation between *g*-shifts in low-spin, rhombic EPR spectra of Fe(III) heme-thiolates and the strength of H-bond donation to thiolate. This relationship may be utilized to better understand how H-bonding controls function in the diverse family of proteins bearing an axial thiolate ligand.

■ ASSOCIATED CONTENT

Supporting Information

The Supporting Information is available free of charge on the ACS Publications website at DOI: 10.1021/acs.inorgchem.9b02506.

Detailed methods for X-ray crystallography and additional crystallographic data, molecular orbital diagrams for hemoprotein models, spectroscopic data for synthesized compounds, and atomic coordinates for geometry-optimized structures (PDF)

Accession Codes

CCDC 1939954 contains the supplementary crystallographic data for this paper. These data can be obtained free of charge via www.ccdc.cam.ac.uk/data_request/cif, or by emailing data_request@ccdc.cam.ac.uk, or by contacting The Cambridge Crystallographic Data Centre, 12 Union Road, Cambridge CB2 1EZ, UK; fax: +44 1223 336033.

■ AUTHOR INFORMATION

Corresponding Author

*Phone: 608-262-0328. Fax: 608-262-6143. E-mail: burstyn@chem.wisc.edu.

ORCID

Matthew R. Dent: 0000-0002-7704-4867
Andrew P. Hunt: 0000-0003-0565-9050
Ilia A. Guzei: 0000-0003-1976-7386

DOI: 10.1021/acs.inorgchem.9b02506
Inorg. Chem. XXXX, XXX, XXX−XXX

Nicolai Lehnert: 0000-0002-5221-5498

Author Contributions

M.R.D. carried out computational analyses and wrote the manuscript. M.W.M. synthesized and characterized ligands and ligand precursors in the lab of J.N.B. A.P.H. developed the methodology for the synthesis of 5-c aryl-thiolate complexes in the lab of N.L. A.P.H., M.W.M., and M.R.D. synthesized and characterized porphyrin complexes. M.M.A. and I.A.G. carried out single crystal X-ray diffraction experiments.

Notes

The authors declare no competing financial interest.

■ ACKNOWLEDGMENTS

We gratefully acknowledge Prof. Thomas Brunold (University of Wisconsin, Madison, Chemistry) for helpful discussions regarding the analysis of computational results. We also thank Prof. Joshua Telser (Roosevelt University) for helpful comments and for providing his version of Prof. Bruce R. McGarvey's original ligand-field theory program, DLSD5. Finally, we thank Prof. Sam Pazicni (University of Wisconsin, Madison, Chemistry), whose dissertation laid the foundation for this work. This research was supported by the National Science Foundation (CHE-1213739 to J.N.B., CHE-1464696 to N.L.). M.R.D. was supported by the NIH/NIGMS under award number T32 GM008293. Instrumentation in Paul Bender Chemical Instrumentation Facility at UW-Madison were supported as follows: Thermo Q Exactive Plus mass spectrometer by NIH 1S10 OD020022-1; Bruker Avance III 500 MHz NMR spectrophotometer by a generous gift from Paul J. and Margaret M. Bender; Bruker EleXsys E500 EPR spectrophotometer by NSF CHE-0741901.

■ REFERENCES

(1) Smith, A. T.; Pazicni, S.; Marvin, K. A.; Stevens, D. J.; Paulsen, K. M.; Burstyn, J. N. Functional divergence of heme-thiolate proteins: A classification based on spectroscopic attributes. *Chem. Rev.* **2015**, *115*, 2532.

(2) Sono, M.; Roach, M. P.; Coulter, E. D.; Dawson, J. H. Heme-containing oxygenases. *Chem. Rev.* **1996**, *96*, 2841.

(3) Yosca, T. H.; Rittle, J.; Krest, C. M.; Onderko, E. L.; Silakov, A.; Calixto, J. C.; Behan, R. K.; Green, M. T. Iron(IV)hydroxide pK(a) and the role of thiolate ligation in C-H bond activation by cytochrome P450. *Science (Washington, DC, U. S.)* **2013**, *342*, 825.

(4) Yoshioka, S.; Tosha, T.; Takahashi, S.; Ishimori, K.; Hori, H.; Morishima, I. Roles of the proximal hydrogen bonding network in cytochrome P450cam-catalyzed oxygenation. *J. Am. Chem. Soc.* **2002**, *124*, 14571.

(5) Galinato, M. G. I.; Spolitak, T.; Ballou, D. P.; Lehnert, N. Elucidating the role of the proximal cysteine hydrogen-bonding network in ferric cytochrome P450cam and corresponding mutants using magnetic circular dichroism spectroscopy. *Biochemistry* **2011**, *50*, 1053.

(6) Lehnert, N. Elucidating second coordination sphere effects in heme proteins using low-temperature magnetic circular dichroism spectroscopy. *J. Inorg. Biochem.* **2012**, *110*, 83.

(7) Mak, P. J.; Yang, Y.; Im, S.; Waskell, L. A.; Kincaid, J. R. Experimental documentation of the structural consequences of hydrogen-bonding interactions to the proximal cysteine of a cytochrome P450. *Angew. Chem., Int. Ed.* **2012**, *51*, 10403.

(8) Krest, C. M.; Silakov, A.; Rittle, J.; Yosca, T. H.; Onderko, E. L.; Calixto, J. C.; Green, M. T. Significantly shorter Fe−S bond in cytochrome P450-I is consistent with greater reactivity relative to chloroperoxidase. *Nat. Chem.* **2015**, *7*, 696.

(9) McQuarters, A. B.; Speelman, A. L.; Chen, L.; Elmore, B. O.; Fan, W.; Feng, C.; Lehnert, N. Exploring second coordination sphere effects in nitric oxide synthase. *J. Biol. Inorg. Chem.* **2016**, *21*, 997.

(10) Hunt, A. P.; Lehnert, N. The thiolate trans effect in heme {FeNO}^{6} complexes and beyond: Insight into the nature of the push effect. *Inorg. Chem.* **2019**.*5*811317

(11) Aono, S.; Ohkubo, K.; Matsuo, T.; Nakajima, H. Redox-controlled ligand exchange of the heme in the CO-sensing transcriptional activator CooA. *J. Biol. Chem.* **1998**, *273*, 25757.

(12) Shelver, D.; Thorsteinsson, M. V.; Kerby, R. L.; Chung, S.-Y.; Roberts, G. P.; Reynolds, M. F.; Parks, R. B.; Burstyn, J. N. Identification of two important heme site residues (Cysteine 75 and Histidine 77) in CooA, the CO-sensing transcription factor of *Rhodospirillum rubrum*. *Biochemistry* **1999**, *38*, 2669.

(13) Dhawan, I. K.; Shelver, D.; Thorsteinsson, M. V.; Roberts, G. P.; Johnson, M. K. Probing the heme axial ligation in the CO-sensing CooA protein with magnetic circular dichroism spectroscopy. *Biochemistry* **1999**, *38*, 12805.

(14) Vogel, K. M.; Spiro, T. G.; Shelver, D.; Thorsteinsson, M. V.; Roberts, G. P. Resonance Raman evidence for a novel charge relay activation mechanism of the CO-dependent heme protein transcription factor CooA. *Biochemistry* **1999**, *38*, 2679.

(15) Poulos, T. L.; Finzel, B. C.; Howard, A. J. High-resolution crystal structure of cytochrome P450cam. *J. Mol. Biol.* **1987**, *195*, 687.

(16) Cupp-Vickery, J. R.; Poulos, T. L. Structure of cytochrome P450 eryF: An enzyme involved in erythromycin biosynthesis. *Nat. Struct. Mol. Biol.* **1995**, *2*, 144.

(17) Ravichandran, K. G.; Boddupalli, S. S.; Hasermann, C. A.; Peterson, J. A.; Deisenhofer, J. Crystal structure of hemoprotein domain of P450BM-3, a prototype for microsomal P450's. *Science (Washington, DC, U. S.)* **1993**, *261*, 731.

(18) Hasemann, C. A.; Kurumbail, R. G.; Boddupalli, S. S.; Peterson, J. A.; Deisenhofer, J. Structure and function of cytochromes P450: a comparative analysis of three crystal structures. *Structure* **1995**, *3*, 41.

(19) Das, P. K.; Chatterjee, S.; Samanta, S.; Dey, A. EPR, Resonance Raman, and DFT calculations on thiolate- and imidazole-bound iron(III) porphyrin complexes: Role of the axial ligand in tuning the electronic structure. *Inorg. Chem.* **2012**, *51*, 10704.

(20) Dey, A.; Jiang, Y.; Ortiz de Montellano, P.; Hodgson, K. O.; Hedman, B.; Solomon, E. I. S K-edge XAS and DFT Calculations on cytochrome P450: Covalent and ionic contributions to the cysteine-Fe bond and their contribution to reactivity. *J. Am. Chem. Soc.* **2009**, *131*, 7869.

(21) Dey, A.; Okamura, T.-a.; Ueyama, N.; Hedman, B.; Hodgson, K. O.; Solomon, E. I. Sulfur K-Edge XAS and DFT calculations on P450 model complexes: Effects of hydrogen bonding on electronic structure and redox potentials. *J. Am. Chem. Soc.* **2005**, *127*, 12046.

(22) Groves, J. T. Key elements of the chemistry of cytochrome P-450: The oxygen rebound mechanism. *J. Chem. Educ.* **1985**, *62*, 928.

(23) Dawson, J. H.; Sono, M. Cytochrome P-450 and chloroperoxidase: Thiolate-ligated heme enzymes. Spectroscopic determination of their active-site structures and mechanistic implications of thiolate ligation. *Chem. Rev. (Washington, DC, U. S.)* **1987**, *87*, 1255.

(24) Behan, R. K.; Green, M. T. On the status of ferryl protonation. *J. Inorg. Biochem.* **2006**, *100*, 448.

(25) Davydov, R.; Im, S.; Shanmugam, M.; Gunderson, W. A.; Pearl, N. M.; Hoffman, B. M.; Waskell, L. Role of the proximal cysteine hydrogen bonding interaction in cytochrome P450 2B4 studied by cryoreduction, electron paramagnetic resonance, and electron−nuclear double resonance spectroscopy. *Biochemistry* **2016**, *55*, 869.

(26) Yosca, T. H.; Ledray, A. P.; Ngo, J.; Green, M. T. A new look at the role of thiolate ligation in cytochrome P450. *JBIC, J. Biol. Inorg. Chem.* **2017**, *22*, 209.

(27) Kerby, R. L.; Youn, H.; Roberts, G. P. RcoM: A new single-component transcriptional regulator of CO metabolism in bacteria. *J. Bacteriol.* **2008**, *190*, 3336.

(28) Bowman, H. E.; Dent, M. R.; Burstyn, J. N. Met104 is the CO-replaceable ligand at Fe(II) heme in the CO-sensing transcription factor *Bx*RcoM-1. *JBIC, J. Biol. Inorg. Chem.* **2016**, *21*, 559.

DOI: 10.1021/acs.inorgchem.9b02506
Inorg. Chem. XXXX, XXX, XXX−XXX

(29) Roberts, G. P.; Youn, H.; Kerby, R. L. CO-sensing mechanisms. *Microbiol. Mol. Biol. Rev.* **2004**, *68*, 453.
(30) Roberts, G. P.; Kerby, R. L.; Youn, H.; Conrad, M. CooA, a paradigm for gas sensing regulatory proteins. *J. Inorg. Biochem.* **2005**, *99*, 280.
(31) Kerby, R. L.; Roberts, G. P. *Burkholderia xenovorans* RcoM*Bx*-1, a transcriptional regulatorsystem for sensing low and persistent levels of carbon monoxide. *J. Bacteriol.* **2012**, *194*, 5803.
(32) Hines, J. P.; Dent, M. R.; Stevens, D. J.; Burstyn, J. N. Site-directed spin label electron paramagnetic resonance spectroscopy as a probe of conformational dynamics in the Fe(III) "*locked-off*" state of the CO-sensing transcription factor CooA. *Protein Sci.* **2018**, *27*, 1670.
(33) Deng, B.; Parthasarathy, S.; Wang, W.; Gibney, B. R.; Battaile, K. P.; Lovell, S.; Benson, D. R.; Zhu, H. Study of the individual cytochrome b5 and cytochrome *b*5 reductase domains of Ncb5or reveals a unique heme pocket and a possible role of the CS domain. *J. Biol. Chem.* **2010**, *285*, 30181.
(34) Silkstone, G. G.; Cooper, C. E.; Svistunenko, D.; Wilson, M. T. EPR and optical spectroscopic studies of Met80X mutants of yeast ferricytochrome c. Models for intermediates in the akaline transition. *J. Am. Chem. Soc.* **2005**, *127*, 92.
(35) Smith, A. T.; Su, Y.; Stevens, D. J.; Majtan, T.; Kraus, J. P.; Burstyn, J. N. Effect of the disease-causing R266K mutation on the heme and PLP environments of the human enzyme cystathionine ß-synthase. *Biochemistry* **2012**, *51*, 6360.
(36) Bohan, T. L. Analysis of low-spin ESR spectra of ferric heme proteins: A reexamination. *J. Magn. Reson.* **1977**, *26*, 109.
(37) Peisach, J.; Blumberg, W. E. Electron paramagnetic resonance study of the high- and low-spin forms of cytochrome P-450 in liver and in liver microsomes from a methylcholanthrene-treated rabbit. *Proc. Natl. Acad. Sci. U. S. A.* **1970**, *67*, 172.
(38) Blumberg, W. E.; Peisach, J. *Probes of Structure and Function of Macromolecules and Membranes*; Academic Press: New York, 1971; Vol. *2*.
(39) Palmer, G. In *The Porphyrins*; Dolphin, D., Ed. Academic Press, Inc.: New York, NY, 1979; Vol. *IV*, p 313.
(40) Barr, I.; Smith, A. T.; Senturia, R.; Chen, Y.; Scheidemantle, B. D.; Burstyn, J. N.; Guo, F. DiGeorge critical region 8 (DGCR8) is a double-cysteine-ligated heme protein. *J. Biol. Chem.* **2011**, *286*, 16716.
(41) Stoll, S.; Schweiger, A. EasySpin, a comprehensive software package for spectral simulation and analysis in EPR. *J. Magn. Reson.* **2006**, *178*, 42.
(42) McGarvey, B. R. Survey of ligand field parameters of strong field d^5 complexes obtained from the *g* matrix. *Coord. Chem. Rev.* **1998**, *170*, 75.
(43) Bendix, J.; Brorson, M.; Schaffer, C. E. Accurate empirical spin-orbit coupling parameters. zeta. nd for gaseous ndq transition metal ions. The parametrical multiplet term model. *Inorg. Chem.* **1993**, *32*, 2838.
(44) Jiang, Y.; Telser, J.; Goldberg, D. P. Evidence for the formation of a mononuclear ferric−hydroperoxo complex via the reaction of dioxygen with an (N4S(thiolate))iron(ii) complex. *Chem. Commun.* **2009**, 6828.
(45) Taylor, C. P. S. The EPR of low spin heme complexes Relation of the t2g hole model to the directional properties of the *g* tensor, and a new method for calculating the ligand field parameters. *Biochim. Biophys. Acta, Protein Struct.* **1977**, *491*, 137.
(46) Neese, F. Software update: The ORCA program system, version 4.0. *Wiley Interdiscip. Rev. Comp. Mol. Sci.* **2018**, *8*, No. e1327.
(47) Frisch, M. J.; Trucks, G. W.; Schlegel, H. B.; Scuseria, G. E.; Robb, M. A.; Cheeseman, J. R.; Scalmani, G.; Barone, V.; Mennucci, B.; Petersson, G. A.; Nakatsuji, H.; Caricato, M.; Li, X.; Hratchian, H. P.; Izmaylov, A. F.; Bloino, J.; Zheng, G.; Sonnenberg, J. L.; Hada, M.; Ehara, M.; Toyota, K.; Fukuda, R.; Hasegawa, J.; Ishida, M.; Nakajima, T.; Honda, Y.; Kitao, O.; Nakai, H.; Vreven, T.; Montgomery, J. A., Jr.; Peralta, J. E.; Ogliaro, F.; Bearpark, M.; Heyd, J. J.; Brothers, E.; Kudin, K. N.; Staroverov, V. N.; Kobayashi, R.; Normand, J.; Raghavachari, K.; Rendell, A.; Burant, J. C.; Iyengar, S. S.; Tomasi, J.; Cossi, M.; Rega, N.; Millam, J. M.; Klene, M.; Knox, J. E.; Cross, J. B.; Bakken, V.; Adamo, C.; Jaramillo, J.; Gomperts, R.; Stratmann, R. E.; Yazyev, O.; Austin, A. J.; Cammi, R.; Pomelli, C.; Ochterski, J. W.; Martin, R. L.; Morokuma, K.; Zakrzewski, V. G.; Voth, G. A.; Salvador, P.; Dannenberg, J. J.; Dapprich, S.; Daniels, A. D.; Farkas, O.; Foresman, J. B.; Ortiz, J. V.; Cioslowski, J.; Fox, D. J. *Gaussian 09*, revision E.01; Gaussian, Inc.: Wallingford, CT, 2009.
(48) Becke, A. D. Density-functional exchange-energy approximation with correct asymptotic behavior. *Phys. Rev. A: At., Mol., Opt. Phys.* **1988**, *38*, 3098.
(49) Perdew, J. P. Density-functional approximation for the correlation energy of the inhomogeneous electron gas. *Phys. Rev. B: Condens. Matter Mater. Phys.* **1986**, *33*, 8822.
(50) Schafer, A.; Horn, H.; Ahlrichs, R. Fully optimized contracted gaussian basis sets for atoms Li to Kr. *J. Chem. Phys.* **1992**, *97*, 2571.
(51) Weigend, F. Accurate Coulomb-fitting basis sets for H to Rn. *Phys. Chem. Chem. Phys.* **2006**, *8*, 1057.
(52) Lee, C. T.; Yang, W. T.; Parr, R. G. Development of the Colle-Salvetti correlation energy formula into a functional of the electron density. *Phys. Rev. B: Condens. Matter Mater. Phys.* **1988**, *37*, 785.
(53) Weigend, F.; Ahlrichs, R. Balanced basis sets of split valence, triple zeta valence and quadruple zeta valence quality for H to Rn: Design and assessment of accuracy. *Phys. Chem. Chem. Phys.* **2005**, *7*, 3297.
(54) Durley, R. C.; Mathews, F. S. Refinement and structural analysis of bovine cytochrome *b*5 at 1.5 A resolution. *Acta Crystallogr., Sect. D: Biol. Crystallogr.* **1996**, *52*, 65.
(55) Ochi, H.; Hata, Y.; Tanaka, N.; Kakudo, M.; Sakurai, T.; Aihara, S.; Morita, Y.; Huber, R. Structure of rice ferricytochrome c at 2·0 Å resolution. *J. Mol. Biol.* **1983**, *166*, 407.
(56) Meier, M.; Janosik, M.; Kery, V.; Kraus, J. P.; Burkhard, P. Structure of human cystathionine *β*-synthase: a unique pyridoxal 5′-phosphate-dependent heme protein. *EMBO J.* **2001**, *20*, 3910.
(57) Tang, S. C.; Koch, S.; Papaefthymiou, G. C.; Foner, S.; Frankel, R. B.; Ibers, J. A.; Holm, R. H. Axial ligation modes in iron(III) porphyrins. Models for the oxidized reaction states of cytochrome P-450 enzymes and the molecular structure of iron(III) protoporphyrin IX dimethyl ester p-nitrobenzenethiolate. *J. Am. Chem. Soc.* **1976**, *98*, 2414.
(58) Verras, A.; Alian, A.; de Montellano, P. R. Cytochrome P450 active site plasticity: attenuation of imidazole binding in cytochrome P450(cam) by an L244A mutation. *Protein Eng., Des. Sel.* **2006**, *19*, 491.
(59) Schmidt, J. R.; Polik, W. F.; WebMO LLC: Holland, MI, USA, 2013; Vol. *2019*.
(60) Griffith, J. S. Binding in hæmoglobin azide as determined by electron resonance: Theory of electron resonance in ferrihæmoglobin azide. *Nature* **1957**, *180*, 30.
(61) Palmer, G. The electron paramagnetic resonance of metalloproteins. *Biochem. Soc. Trans.* **1985**, *13*, 548.
(62) Ueyama, N.; Nishikawa, N.; Yamada, Y.; Okamura, T.-a.; Nakamura, A. Cytochrome P-450 model (Porphinato)(thiolato)iron-(III) complexes with single and double NH···S hydrogen bonds at the thiolate site. *J. Am. Chem. Soc.* **1996**, *118*, 12826.
(63) McDaniel, D. H.; Brown, H. C. An extended table of hammett substitutent constants based on the ionization of substituted benzoic acids. *J. Org. Chem.* **1958**, *23*, 420.
(64) Shinkai, H.; Maeda, K.; Yamasaki, T.; Okamoto, H.; Uchida, I. Bis(2-(Acylamino)phenyl) disulfides, 2-(Acylamino)benzenethiols, and S-(2-(Acylamino)phenyl) alkanethioates as novel inhibitors of cholesteryl ester transfer protein. *J. Med. Chem.* **2000**, *43*, 3566.
(65) Sarma, B. K.; Mugesh, G. Redox regulation of protein tyrosine phosphatase 1B (PTP1B): A biomimetic study on the unexpected formation of a sulfenyl amide intermediate. *J. Am. Chem. Soc.* **2007**, *129*, 8872.
(66) Byrn, M. P.; Strouse, C. E. Porphyrin sponges. Inversion disorder and inversion twinning in lattice clathrates based on five-coordinate metallotetraarylporphyrin complexes. *J. Am. Chem. Soc.* **1991**, *113*, 2501.

DOI: 10.1021/acs.inorgchem.9b02506
Inorg. Chem. XXXX, XXX, XXX−XXX

(67) Paulat, F.; Lehnert, N. Electronic structure of ferric heme nitrosyl complexes with thiolate coordination. *Inorg. Chem.* **2007**, *46*, 1547.
(68) Blumberg, W. E.; Peisach, J. Low-spin compounds of hemoproteins. *Adv. Chem. Ser.* **1971**, *100*, 271.
(69) Gadsby, P. M. A.; Thomson, A. J. Assignment of the axial ligands of ferric ion in low-spin hemoproteins by near-infrared magnetic circular dichroism and electronic resonance spectroscopy. *J. Am. Chem. Soc.* **1990**, *112*, 5003.

DOI: 10.1021/acs.inorgchem.9b02506
Inorg. Chem. XXXX, XXX, XXX−XXX